Analysis of Vascular Homogeneity and Anisotropy on High-Resolution Primate Brain Imaging

Pol Kennel,[1] Caroline Fonta,[2] Romain Guibert,[1] and Franck Plouraboué[1]*

[1]*Institut de Mécanique des Fluides de Toulouse (IMFT), Université de Toulouse, CNRS, INPT, UPS, Toulouse, France*
[2]*Brain and Cognition Research Center (CerCo), CNRS-University of Toulouse UPS, F-31052 Toulouse Cedex, France*

Abstract: Using a systematic investigation of brain blood volume, in high-resolution synchrotron 3D images of microvascular structures within cortical regions of a primate brain, we challenge several basic questions regarding possible vascular bias in high-resolution functional neuroimaging. We present a bilateral comparison of cortical regions, where we analyze relative vascular volume in voxels from 150 to 1000 μm side lengths in the white and grey matter. We show that, if voxel size reaches a scale smaller than 300 μm, the vascular volume can no longer be considered homogeneous, either within one hemisphere or in bilateral comparison between samples. We demonstrate that voxel size influences the comparison between vessel-relative volume distributions depending on the scale considered (i.e., hemisphere, lobe, or sample). Furthermore, we also investigate how voxel anisotropy and orientation can affect the apparent vascular volume, in accordance with actual fMRI voxel sizes. These findings are discussed from the various perspectives of high-resolution brain functional imaging. *Hum Brain Mapp 00:000–000, 2017.* © 2017 Wiley Periodicals, Inc.

Key words: cortex; marmoset monkey; vessel density; CBV; micro-CT; voxel size; vascular homogeneity; fMRI

INTRODUCTION

Considerable progress has been made in the resolution of functional brain imaging during the last two decades. It may seem natural to think that, the higher the resolution, the better the disclosure of the brain's function. However, consideration of the influence of neuro-vascular heterogeneity sampled at small scale, suggests that this viewpoint should be tempered. As quoted in Goense et al. [2016], "*features and processes that were previously lumped into a single voxel become spatially distinct at high resolution*." When the characteristic size of the underlying vascular vessels becomes comparable with voxel size, modifications can be expected in the local signal. Hence, depending on the cortex region considered, the local cortex orientation, and/or the voxel position within the brain, some specific vascular contribution might impair or bias functional signals when spatial resolution increases. For this reason, ultra-high-resolution functional brain imaging also brings with it new methodological issues, that are worth considering, but were previously discarded at much lower resolution. Among the above mentioned methodological issues challenged by downscaling the fMRI resolution, the first one we will consider is the homogeneity of the cerebral blood volume (CBV) among various voxels. How CBV compares, at high resolution, in various cortical areas, as qualitatively described in the human brain [Duvernoy, 1999; Reina-De

Additional Supporting Information may be found in the online version of this article.

*Correspondence to: F. Plouraboué; Institut de Mécanique des Fluides de Toulouse (IMFT UMR 5502), Université de Toulouse, CNRS, INPT, UPS, Toulouse, France. E-mail: fplourab@imft.fr

Received for publication 17 February 2017; Revised 28 July 2017; Accepted 2 August 2017.

DOI: 10.1002/hbm.23766

Published online 00 Month 2017 in Wiley Online Library (wileyonlinelibrary.com).

La Torre et al., 1998] depending on voxels size is not clearly known. Quantitative data, mainly originating from animal studies, show that vascular density varies among cortical areas [Michaloudi et al., 2005; Weber et al., 2008; Tsai et al., 2009].

A second issue is related to the influence of the orientation of the voxel relative to the local cortex surface orientation. Measurements of cerebral perfusion, using dynamic susceptibility contrast magnetic resonance imaging, mostly rely on the assumption of isotropic vascular architecture. Nevertheless, early high-magnetic-field gradient-echo fMRI studies [Ogawa et al., 1990] pin-point the effects of susceptibility contrast associated with vessels producing intravoxel dephasing of the water signals, as recently confirmed in spin-echo fMRI [Vignaud et al., 2006]. More recent fMRI studies pointed out strong dependence of cerebral blood flow (CBF) and CBV on tissue orientation [Hernández-Torres et al., 2016]. Arteriolar and venous vessels display preferential orientations, either in grey matter orthogonally to the cortex surface, or in white matter, following myelin fiber tracts. Most penetrating vessels in cortical grey matter, which carry almost half of the CBV [Risser et al., 2009], are oriented perpendicularly to the local pial surface. Concerning the capillaries carrying the other half of the CBV, in marmosets as in humans [Lauwers et al., 2008; Risser et al., 2009], their orientation is always highly scattered. It is, therefore, interesting to investigate whether vessel orientation could influence local CBV sampling in isotropic and anisotropic voxels at ultrahigh resolution.

In this study, we use micron-sized high-quality synchrotron tomography images, spanning several tens of cubic millimeters, to provide a ground-truth base for CBV: the quality (high signal-to-noise ratio of vessel contrast) of the microvascular signal permits the extraction of binary images (segmented vessel/tissue) so that CBV can reliably be evaluated in any subvolume. This has been performed by injecting a suitable contrast agent in all vessels from pial vessels to small capillaries so that they are easy to segment from the background. Using a data set of images, over 20 samples extracted from identified cortical zones of both hemispheres of one primate cerebral cortex, we are able to provide detailed quantitative estimate of CBV in white and grey matter. We developed a specific image analysis workflow for the segmentation of grey and white matter regions, inside which we estimated CBV for various voxel sizes and orientations. We then described the different grey and white matter regions in the cortical zones of both cerebral hemispheres. Our aim is to

- provide new data on hypothetical CBV disparity between cortical areas/lobes and between cerebral hemispheres, in the grey and in the white matters for extensive range of voxel sizes;
- analyze how voxel orientations affect CBV homogeneity, and provide a first estimation of the resulting anisotropy of the magnetic field susceptibility-contrast induced response within the tissue (i.e., expected changes in the local tissue magnetic field resulting from the presence of high susceptibility contrast vessels plunged into a uniform external static magnetic field vector $\mathbf{B}_0$).

MATERIALS AND METHODS

Preparation and Typology of Samples

Sample preparation and positioning

The samples were extracted from a 24-month-old female marmoset *Callithix jacchus* born in the accredited (n°31 555 01) primate center in CerCo-UMR5549. The procedures were in accordance with the recommendations of the European Economic Community (directive 2010/63/UE) and the National Committee for Ethical Reflection on Animal Testing (authorization number: MP/07/3810/09). The animal, under lethal anesthesia, was perfused with a suspension of barium sulfate as detailed in (Risser et al., 2007, 2009). With the help of anatomical landmarks (in particular the lateral sulcus) and marmoset brain atlas (Palazzi and Bordier, 2008; Paxinos et al., 2012), samples were removed perpendicularly to the brain surface, using a cylindrical biopsy punch (3 mm internal diameter), in different cortical regions, symmetrically in both hemispheres. Samples were numbered from 1 to 10 for the left hemisphere and 11 to 20 for the right. Sampling targeted the occipital lobe, the parietal lobe, the temporal lobe, and the frontal lobe (Table I and Fig. 1). Localization of the samples extracted from the cortex (in defined cortical areas) was refined, a posteriori, on histological sections of the remaining brain on the basis of the staining patterns of multiple markers. Traditional Nissl and myelin staining methods in addition to histoenzymology to alkaline phosphatase and cytochrome oxidase activity and immunohistochemistry to neurofilaments have been used. The cerebral hemispheres were sectioned in a sagittal plane in order to visualize several sampling points on the same section, and all the sections from the same hemisphere were processed in parallel for each type of staining. The position of each sample was identified from the fusion of the specific areal and laminar information provided by each marker in its surrounding cortex. This identification was indicative and should be considered as a spotting of the samples, for several reasons. Marmoset cortical areas, especially those located in the frontal lobe, have a small areal size, which can be much smaller than the size of the extracted samples. Therefore, samples can lie over several cortical areas. Table I indicates the marmoset areas homologous to Brodmann cortical areas surrounding the samples, and consequently their most appropriate localization. Using the information synthesized in Table I, we manually repositioned the studied samples on a marmoset brain atlas for illustration (Fig. 1).

TABLE I. Characteristics of the grey-matter regions of the 20 samples

	Left hemisphere			Right hemisphere		
Cerebral lobe	Sample	Grey matter 1	Grey matter 2	Sample	Grey matter 1	Grey matter 2
Frontal/frontoparietal	**1**	Areas 3-4 (frontoparietal)	n.a.	**11**	Areas 4-6 (frontal)	n.a.
Occipital	**2**	Area 17 (operculum)	Area 17 (calcarine sulcus)	**12**	Area 17 (operculum)	Area 17 (calcarine sulcus)
Temporal	**3**	Inferotemporal cortex	n.a.	**13**	Inferotemporal cortex	n.a.
Occipitoparietal	**4**	Area 18 dorso medial visual area	Area 17 (calcarine sulcus)	**14**	Dorsomedial visual area	Area 17 (calcarine sulcus)
Occipital	**5**	Area 17 (operculum)	Area 17 (calcarine sulcus)	**15**	Area 17 (operculum)	Area 17 (calcarine sulcus)
Occipital	**6**	Areas 17/18	Area 17 (calcarine sulcus)	**16**	Areas 17/18	n.a.
Occipital	**7**	Area 17 (operculum)	n.a.	**17**	Area 17 (operculum)	n.a.
Frontal	**8**	Areas 6-8-46	n.a.	**18**	areas 46-47	n.a.
Frontal	**9**	Areas 8-9-10-46	n.a.	**19**	n.a.	n.a.
Parietal	**10**	Posterior parietal area	n.a.	**20**	Posterior parietal area	n.a.

n.a = non available.

Histology

After sample extraction, serial parasagittal sections (40 μm thick) were collected individually and placed in rotation in a series of wells filled with adequate buffers for subsequent staining. Thus alternate sections were reacted for several markers:

- *Histochemistry*: 26 sections (left hemisphere) and 21 sections (right hemisphere) were used for Nissl staining. Ten sections per hemisphere were reacted for myelin according to a protocol modified from Gallyas (Gallyas, 1978; Fonta et al., 2004; Negyessy et al., 2011).
- *Histoenzymology*: alkaline phosphatase activity (AP) and cytochrome oxidase activity (CO) were revealed according to Fonta et al. (Fonta et al., 1997, 2004; Fonta and Imbert, 2002). Twenty-six sections (left hemisphere) and 21 sections (right hemisphere) were stained for each of the two markers.

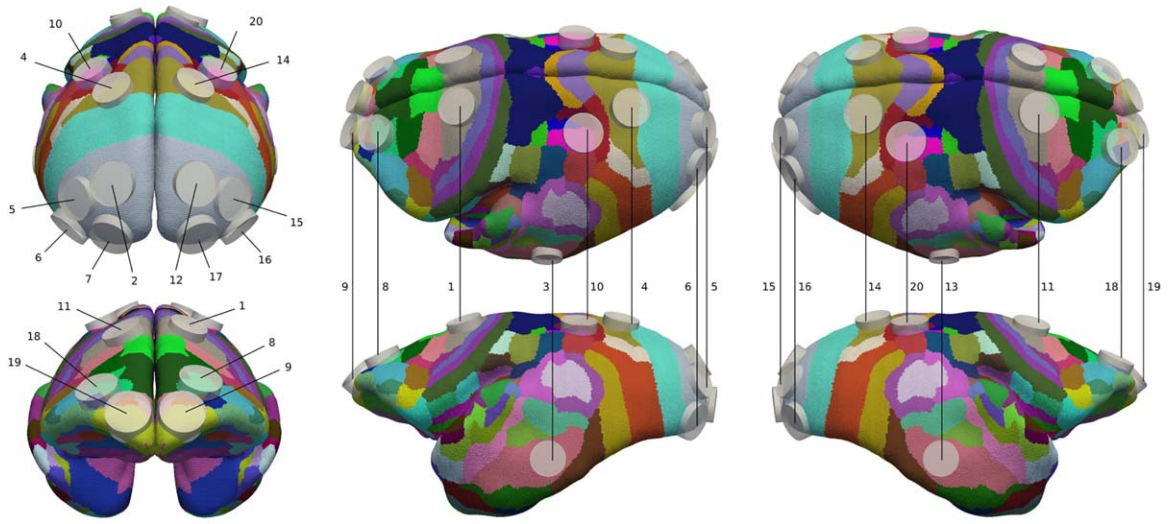

Figure 1.

Locations of Samples #1–#20 on the marmoset cortical surface using a functional atlas that shows areas in random colours (adapted from Paxinos et al. [2012]). The postpositioning of the sample cylinder was performed manually, using all the available histological and typological information. Left: posterior (top) and anterior (bottom) views. Middle: left hemisphere. Right: right hemisphere (dorsal: top row view; lateral: bottom row view). [Color figure can be viewed at wileyonlinelibrary.com]

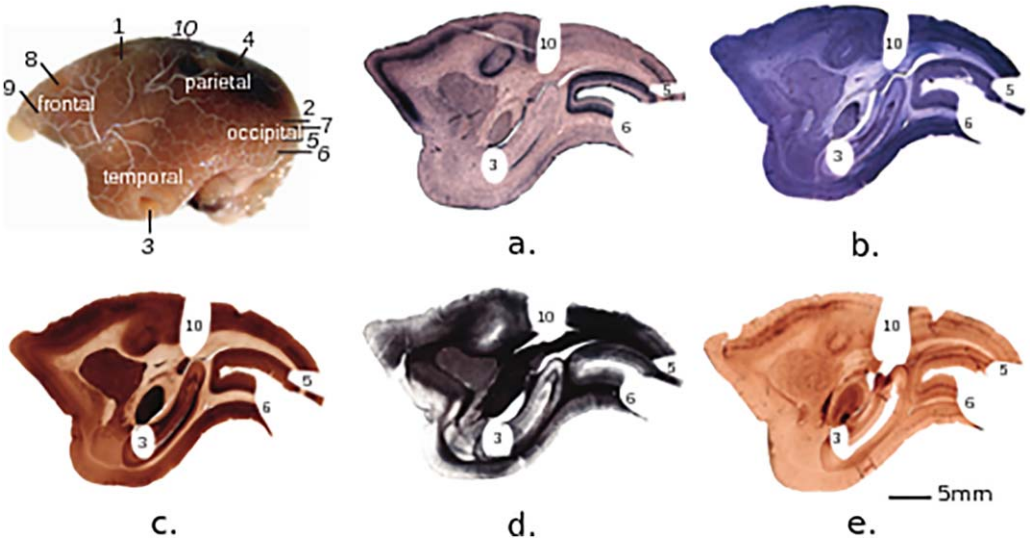

Figure 2.
Serial histological sections of the marmoset left hemisphere stained for (**a**) AP activity, (**b**) Nissl, (**c**) CO activity, (**d**) myelin, and (**e**) neurofilaments (SMI-32). The holes generated by the cylindrical punch sampling in different brain lobes are visible and the corresponding sample number is indicated (only 4 samples are shown here). [Color figure can be viewed at wileyonlinelibrary.com]

- *Immunohistochemistry*: neurofilaments (NF) were detected on 12 sections per hemisphere by using the mouse monoclonal antibody SMI-32 (Covance, Rueil Malmaison, France) (1/4000 for the right hemisphere to 1/6000 for the left hemisphere for 48 h). The biotinylated secondary antibody was applied (1/500) for 2 h. Sections were reacted with the avidin–biotin HRP complex and the reaction product was visualized with diaminobenzidine dissolved in buffer with H_2O_2.

Stained sections were dehydrated and mounted in DPX medium. Images were acquired with a Leica microscope (DMP, Leica Microsystemd, Nanterre, France) and assembled using Mosaic software (Explora Nova®, La Rochelle, France). Figure 2 exemplifies the sample location method (see Supporting Information, SM1 for an overview of staining characteristics).

Image Acquisition and Preprocessing

Brain samples were dehydrated then PEG-embedded to be imaged with a synchrotron X-ray beam at the European Synchrotron Radiation Facility (ESRF) (Plouraboué et al., 2004). The spatial resolution was isotropic and equal to 1.4 μm within a total field view of 2.8×2.8 mm^2 in the vertical and horizontal directions. With this setup, samples were imaged using from two to six vertical scans with a small overlapping region (a few tens of voxels) in the vertical direction, resulting in a total vertical size ranging from 5 to 15 mm. Thus, on one hand, the alignment of the various images in the horizontal direction was perfect (with accuracy much smaller than the voxel size). On the other hand, a correlation peak technique was used to provide the vertical translation between successive scans along the vertical direction. The preprocessing of 3D images consisted of two successive steps [Risser et al., 2007, 2009]. The merged 3D images were binarized using a hysteresis thresholding technique. The resulting binary image was then subjected to conventional 3D erosion-dilation morphological operator processes. Erosion-dilation operators can be visualized as coating or etching the white voxel surfaces so that their surface expands or contracts. These operations enable artificial islands to be eliminated both inside the vessels (black island inside white voxels) and outside the vessels (white island inside black background) (see Shih [2009] for more details).

Reduction of the sample volume due to dehydration was quantified by calculating the ratio between the initial diameter of the sample (3 mm) and the diameters measured on the X-ray images, assuming homogeneous reduction in the whole sample [Risser et al., 2007, 2009]. An average reduction factor of 2.6 ± 0.1 was found and used to scale all measurements over all samples.

The resulting 3D binarized images are illustrated in Figure 3 for Sample #4 initially obtained from two scans. These binarized images were considered as "original images" for the new processing proposed and described in Supporting Information, 2. Figure 3 shows that our protocol of high resolution synchrotron tomography after

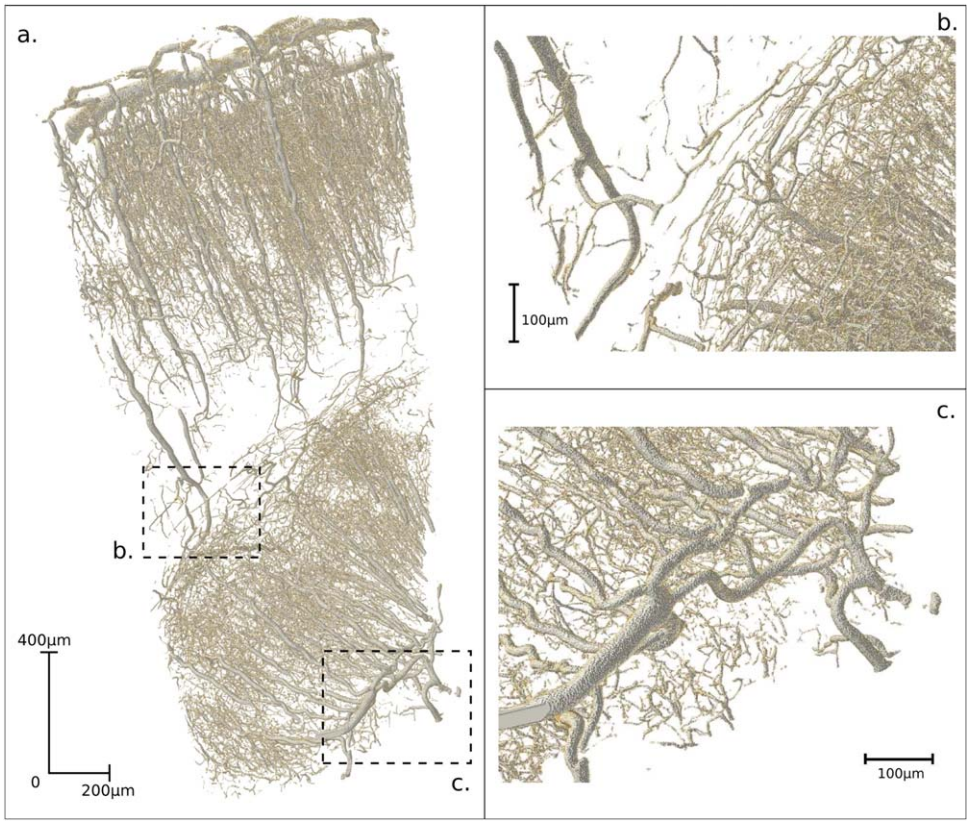

Figure 3.

Illustration of one binarized reconstructed sample (#4). (**a**) Projection view of the vascular structures exhibits two grey matter regions: one on the upper left, the other on the lower right. The reticulated network of the pial vessels that are the roots of penetrating arterioles and veinules branching through the cortex can be distinguished in the sample extremities (see insert in (**c**)). Rare connection between two grey-matter regions by some large penetrating vessels can be observed from the upper grey region into the lower one (inset in **b**). [Color figure can be viewed at wileyonlinelibrary.com]

injection of a contrast agent permitted the entire microvascular hierarchy of vessels (i.e., arteries, veins and capillaries) to be imaged at micron resolution. As the signal-to-noise ratio of these images was very high, binarization provided a direct way to measure the presence of vessels at any location. The relative vascular volume was then easily obtained by computing the volume covered by vessel voxels in each chosen volume of brain tissue. It can be considered as corresponding to a local cerebral blood volume (CBV; expressed in ml of blood/100 g tissue).

Quantitative Characterization of Grey- and White-Matter Regions

Details associated with the grey and white region segmentation are given in Supporting Information, SM2. Given the semantically labeled regions resulting from the segmentation procedure, we extracted two main measurements associated with grey and white matters: the relative vascular volume inside voxels (representing the CBV) and the thickness of the segmented regions. Measuring the thickness required not only the segmentation of a given region but also the definition of a reference axis, along which the average extension of the region was evaluated. As not all tissue samples were exactly aligned with the vertical z axis, a method was needed to determine the reference orientation of the regions.

Evaluation of sample orientation

Let us define $\mathbf{u}_{\mathrm{perf}}$ as the orientation direction of the sample to be estimated from the average orientation of penetrating vessels using image analysis tools. The mean orientation of perforating vessels can be evaluated using a Hessian-based vesselness enhancement known as Frangi's filter [Frangi et al., 1998]. First, one needs to compute the Hessian matrix, H_s, of the original vessel image using different scales, s, where the scale space is built up from a Gaussian blur with a specified standard deviation range, σ_s. Then the eigenvalues λ_k, with $k = 1, 2, 3$ of H and the

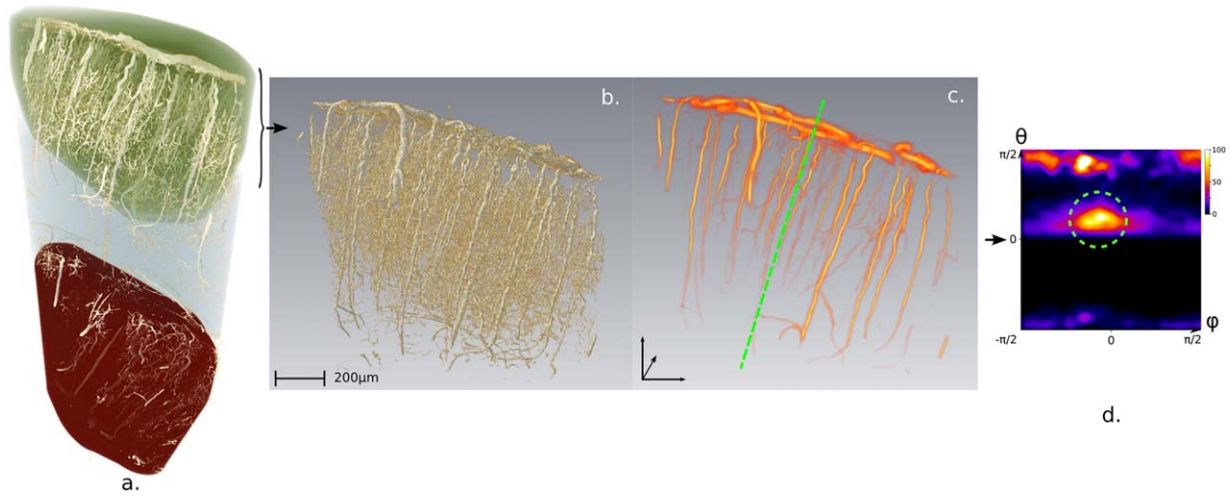

Figure 4.

Identification of the main orientation of perforating vessels with Hessian-based filtering. (**a**) Segmented image, (**b**) top grey region extracted, (**c**) corresponding vesselness map calculated with Frangi's enhancement method corresponding to a scale space adapted to pial and penetrating vessels, and (**d**) two-dimensional orientation histogram corresponding to polar (φ) and azimuthal (θ) angles (Fig. 5) of vessels highlighted by the vesselness map. [Color figure can be viewed at wileyonlinelibrary.com]

corresponding eigenvectors $\mathbf{u}_k$ allow a morphological descriptor, having three principal directions, to be defined at each voxel location (x, y, z). Ideal tubular, and thus vessel-like, structures are characterized by $|\lambda_1| \approx 0$, $|\lambda_1| \ll |\lambda_2|$ and $\lambda_2 \approx \lambda_3$. Frangi has designed a vesselness function $v(\lambda_1, \lambda_2, \lambda_3)$ which sets high values for highly tubular shapes. As $\mathbf{u}_k$ vectors form an orthogonal base projection, $\mathbf{u}_1$ represents the direction for which there is no variation of intensity inside the tube, that is, the vessel orientation. To identify the foremost orientation of the perforating vessels, we used a scale space, s, chosen in the range of vessel diameters (typically $\sigma_s \in [1: 15]$ µm). Vesselness $v(s, x, y, z)$ was then computed for each scale s. The maximum vesselness value over scales and the corresponding local orientation vector $\mathbf{u}_1 \equiv (u_{1x}, u_{1y}, u_{1z})$ were kept. From this, we built up the two-dimensional histogram $C_{i,j}$ defined by

$$C_{i,j} = \sum_{x,y,z} \begin{cases} \max_{s\in[s_{\min},\ s_{\max}]} v(s,x,\ y,z) & \text{if } \varphi = i \text{ and } \theta = j \\ 0 & \text{else} \end{cases}$$

$$\varphi = \arctan\left(\frac{\mathbf{u}_{1y}}{\mathbf{u}_{1x}}\right) \text{ and } \theta = \arctan\left(\sqrt{\frac{\left(\mathbf{u}_{1x}^2 + \mathbf{u}_{1y}^2\right)}{\mathbf{u}_{1z}^2}}\right)$$

Figure 4c displays the vesselness map obtained from the cortical region shown in Figure 4b, resulting from the segmentation of the top region of Figure 4a. The corresponding orientation histogram of each local orientation vector $\mathbf{u}_1$ is then illustrated in Figure 4d, which then enables the foremost orientation of the penetrating vessels $\mathbf{u}_{\text{perf}}$ to be inferred. As histogram $C_{i,j}$ is weighted using the vesselness value instead of a simple count, the highest scored angles in this map correspond to the precise region orientation where vesselness reaches the highest values. In our samples, using a suitable scale space, two main vessel types were generally identified as having the highest vesselness values: perforating vessels and vessels of the pia matter. As shown in Figure 4d, perforating and pial vessel orientations could be clearly identified from histogram $C_{i,j}$ as being associated with θ values that were either close to 0 or $\pi/2$. According to the location of the sample, perforating vessels in the cerebral cortex were more or less closely parallel to each other. A foremost orientation of the unit vector $\mathbf{u}_{\text{perf}}$ associated with polar and azimuthal angles $(\varphi,\theta)_{\text{perf}}$ could be extracted from the location of the maximum of $C_{i,j}$. Samples for which no clear perforating vessel orientation was observed were disregarded to avoid a biased reference orientation which would have resulted in an inadequate estimation of thickness.

Voxel size and orientation

To address the questions of homogeneity and isotropy of the vascular networks inside the cortical tissue, we calculated the relative vascular volume in voxels of growing size, either isotropic or anisotropic, taking into account the effect of voxel orientation in reference to the penetrating vessel orientation.

Voxel size. We defined a voxel (spatial) sampling size (which is much larger than the voxel size of our original

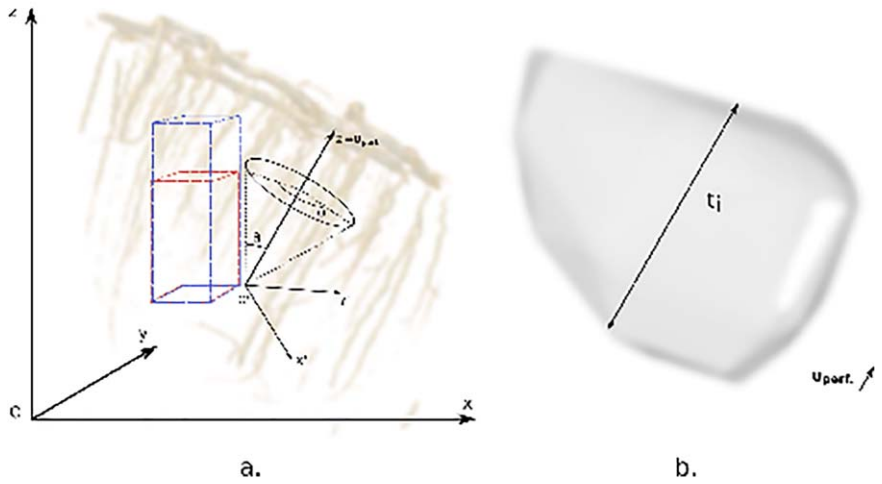

Figure 5.

Orientation of an imaging-voxel inside a grey matter region. (**a**) The relative base ($O'X'Y'Z'$) defined by the orientation of the perforating vessels $\mathbf{u}_{perf}$ is illustrated, making polar angle θ with the small (red) or the large (blue) imaging voxels. (**b**) Illustration of one of the chord-lengths t_i measured in the region hull (the grey shape corresponds to the convex hull of the grey matter region in (a)) used for the thickness estimation. [Color figure can be viewed at wileyonlinelibrary.com]

X-ray tomography images) that will subsequently be referred to as the imaging-voxel. This imaging-voxel can be either isotropic or anisotropic since most voxels used in fMRI studies are indeed anisotropic. More precisely, imaging-voxels are defined from $N \times N \times M$ 3D windows within which the vascular volume is evaluated. M/N represents the anisotropy or the aspect ratio of the imaging-voxel which is generally the ratio between slice resolution and in-plane one.

The orientation of the imaging-voxel grid used for measurement has to be designed with care for a maximum number of imaging-voxels to lie inside (without intersection with the segmented region boundaries) a given (possibly of complex) 3D region (segmented as grey or white matter). This is especially true when large imaging-voxels are to be used. In this case, it is critical to maximize the headcount of imaging-voxels arranged within a given region since, sometimes, only a small number falls inside this region depending on its volume and shape (cf. Figure 5a for illustration). Note that we only consider imaging-voxels totally fitting into each region (partly overlapping imaging-voxels are disregarded). Hence, to find the best location for the grid coordinates, we perform a greedy search to find the optimal grid shift to maximize the number of imaging-voxels in each sample.

Considering the literature from the last 15 years in human and nonhuman primate fMRI studies, voxel volumes are found to be between 0.045 and 77.7 mm^3, the best in-plane resolution being 150×150 μm^2. The aspect ratio (i.e., M/N) ranges between 0.7 and 13.3 but most studies use voxels having an aspect ratio between 1 and 3. Therefore, we specifically investigate the influence of the voxel sizes ranging from 150×150 μm^2 to 1000×1000 μm^2, in plane, and with an aspect ratio between 1 and 3.

Voxel orientation. When measuring the relative vascular volume using anisotropic imaging-voxels, we wish to evaluate the influence of imaging-voxel relative orientation to the penetrating vessels $\mathbf{u}_{perf}$ defined in the previous section. Thus, we define a range of relative polar and azimuthal angles $(\varphi–\varphi_{perf}, \theta–\theta_{perf})$ respectively, with $\varphi \in [0°;370°]$ and $\theta \in [0°;170°]$ for the relative orientation of the imaging-voxel. Vascular volume measurements are performed every 20° for φ and every 10° for θ, which is a good compromise between capturing relevant information and avoiding noisy fluctuations. Obviously, as we compute the relative orientation of any vector to the orientation of $\mathbf{u}_{perf}$, the pair $(\varphi = 0°, \theta = 0°)$ is the angles associated with the orientation of $\mathbf{u}_{perf}$ in each region, as illustrated in Figure 5. As we expect the relative vascular volume not to depend on the azimuthal angle φ, as the main relevant orientation angle is the penetrating vessel one, we concentrate our analysis on variations regarding shifts of the polar angle θ, and merge the vessel volumes extracted over the varying φ for each θ value.

Measurement of regional thickness

We considered the average orientation of penetrating vessels, which is normal to the cortex surface, as the reference direction to be considered for measuring region thickness. Choosing the unit vector $\mathbf{u}_{perf}$ obtained in the section

"Evaluation of sample orientation" as the reference axis associated with the foremost orientation of penetrating vessels for each cortical grey matter, we then define the thickness as being the average of the chord-lengths t_i measured over the region parallel to the orientation of this unit vector $\mathbf{u}_{perf}$, as depicted in Figure 5b (the number of chords corresponds to the maximum number of possible discrete chords in the region).

Statistics

As most of the data collected were not normally distributed, all statistical tests were chosen as nonparametric (Kruskall–Wallis and Kolmogorov–Smirnov tests). P values lower than 0.05 were taken to indicate significant differences. The decision to perform statistical tests on distributions, and not average values, also resulted from the observation that, in most cases (as exemplified by Fig. 9), we did not observe Gaussian distributions.

Estimation of Magnetic Field Inhomogeneity From the Presence of Penetrating Vessels

This section briefly describes how we estimate the magnetic susceptibility contrast emerging from the contributions of cerebral vessels. As capillaries are almost isotropically oriented, their influence onto with susceptibility contrast induced static magnetic field inhomogeneity is considered to be isotropic. Static magnetic field $\mathbf{B}_0$ defines a "natural" direction/orientation. In the following, as in NMR conditions, the axial plane of images is generally orthogonal to the applied constant magnetic field $\mathbf{B}_0$, the principal axis of imaging-voxels (the slice direction) will be considered parallel to $\mathbf{B}_0$. Hence, we do not consider oblique plane imaging, tilted away from the transverse plane (in order to focus on the quantification of the "worst" case scenario). For this reason, we will consider imaging-voxel "orientation" as being synonymous with static field $\mathbf{B}_0$ direction, to discuss the effect of vessel's relative orientation to voxels. Approximately half of the CBV in a primate brain is provided by capillaries while the other half is related to highly oriented penetrating vessels (Risser et al., 2009). Hence, the influence of penetrating vessels on the static susceptibility contrast magnetic field inhomogeneity cannot be considered as isotropic. Penetrating vessels generate highly anisotropic magnetic perturbation, as opposed to capillaries. We quantify this anisotropic field inhomogeneity, whilst disregarding the isotropic one.

Our aim is twofold: (i) to estimate the magnetic field inhomogeneity associated with the presence of penetrating vessels having a given orientation to the static magnetic field, and (ii) to compute how such magnetic perturbations are sampled by anisotropic voxels, elongated along the applied magnetic field $\mathbf{B}_0$. A distinctive feature of almost all fMRI setups is that they sample their signals in noncubic voxels, the main axis (the slice direction, generally being rostro-caudal) of which is perpendicular to the axial (transverse) plane of acquisition. As this axial plane is generally almost orthogonal to the applied constant magnetic field $\mathbf{B}_0$, the principal axis of the rectangular cuboid voxels is almost parallel to $\mathbf{B}_0$. Therefore, in the following, we will identify the polar angle θ, defined in the section "Voxel size and orientation", as the angle between the orientation of penetrating vessels and the direction of the principal axis of the cuboid voxels (cf. Figure 5), as also being the angle between the penetrating vessels orientation and $\mathbf{B}_0$.

To estimate the magnetic response inhomogeneity, we consider the linear superposition of vessel responses as, for example, in Pannetier et al. [2013]. For this, we estimate the cylinder that best fits each penetrating vessel. This is performed by thresholding the vesselness map described in the section "Evaluation of sample orientation," so as to obtain a reliable binary image of large vessels with diameters estimated between 35 and 90 μm. Then the skeletonization procedures described in Risser et al. [2008] are used to obtain a vectorized description of each vessel, providing a sensible evaluation of local diameter along the lineic skeleton. Then an average tube, having an averaged diameter and orientation, is estimated as illustrated in Figure 6b. Each vessel is then manually typed between veins and arteries with an approximated 1/3 ratio (one over three penetrating vessels are veins, Guibert et al. [2012]). A corresponding tissue/vessel susceptibility contrast $\Delta_\chi AT = 10^{-7}$ IU, resp. $\Delta_\chi VT = 2.7 \times 10^{-7}$ IU is then attributed to arteries resp. veins [Lin et al., 2010; Wang et al., 2000]. Using classical formulae (e.g., Ogawa et al. [1993]) for the magnetic perturbations associated with an infinite straight cylinder making a given angle with the applied uniform magnetic field $\mathbf{B}_0$ and having a susceptibility contrast $\Delta\chi$ between the vessel and the surrounding tissue, we compute the resulting contribution, at each location, to the dimensionless magnetic perturbation $\delta B/B_0$, where B_0 is the modulus of the applied magnetic field $\mathbf{B}_0$. Then within each (possibly anisotropic) imaging-voxel (like ones illustrated in Fig. 5), we compute the average magnetic perturbation when the angle θ varies between 0 and $\pi/2$. The imaging-voxel sizes are the same as those used for vascular volume measurements. The statistics related to these computations are reported in results section.

RESULTS

The segmentation procedures used provided appropriate grey- and white-matter delimitations for measurements in a large majority of samples (as illustrated in Fig. 7 for a few samples in both cerebral hemispheres). Regions with abnormal shapes or contents resulting from the segmentation were discarded (e.g., very thin white regions or grey regions containing large empty areas). Regions of interest for our study on grey matter were then selected by

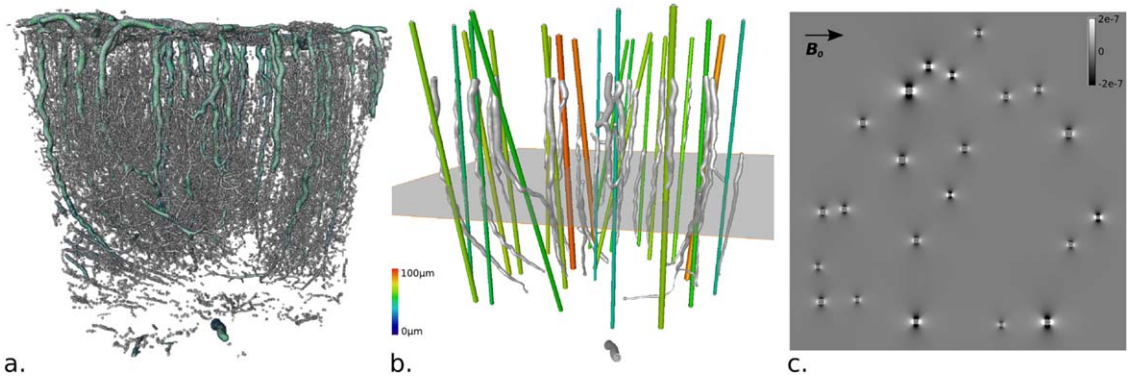

Figure 6.

(**a**) Volume rendering of the entire set of vessels of the upper grey matter region of Sample #18. (**b**) Superposition of the penetrating vessels obtained from image (a) (in grey) with their "average" straight tubes (having their average diameter) in colour from blue to red, 35–90 µm. (**c**) Visualization of the magnetic perturbation field $\delta B/B_0$ in the plane illustrated in (b), for a transverse magnetic field $\mathbf{B}_0$ (values $[-2 \times 10^{-7}, 2 \times 10^{-7}]$ are coded from black to white). [Color figure can be viewed at wileyonlinelibrary.com]

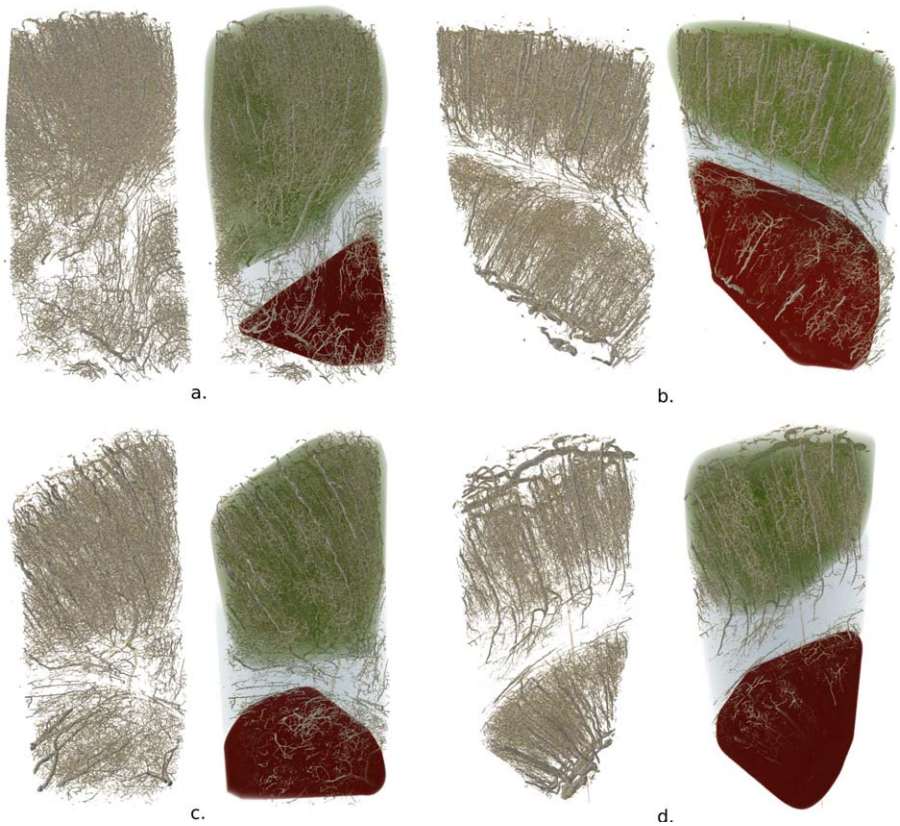

Figure 7.

Volume rendering of vessels (left) and their regional segmentation (right) in different samples (a,b,c,d subplots). Locations of grey-matter (green or red) and white-matter (light blue) regions are illustrated from our segmentation strategy for various samples. (**a**) Sample #9. Right: the upper green region is grey matter, and the lower red region is mainly subcortical tissue. (**b**) Sample #12. Right: both upper green region and lower red region are cortical grey matter. (**c**) Sample #11. Right: the upper green region is cortical grey matter and the lower red region is subcortical matter. (**d**) Sample #14. Right: both upper green region and lower red region are cortical grey matter. [Color figure can be viewed at wileyonlinelibrary.com]

keeping only cortical structures (e.g., Fig. 7b,d where two regions of cortical grey matter, grey #1 (upper, green) and grey #2 (lower, red) can be identified) and omitting subcortical ones (e.g., red regions in Fig. 7a,c). Cortical areas in the grey matter regions were identified using the histological approach, by their location and the typical pattern of their vascularization, that is, large vessels penetrating or emerging from the tissue along a right angle.

Relative Vascular Volume Versus Voxel Size

In this section, we focus on results for cubic imaging-voxels, whose size, similar in any direction, ranges from 150 to 1000 μm. For each resolution, we analyzed 20 samples, paired in numbering as n (resp. $n+10$) for the left (resp. right) hemisphere, from $n=1$ to $n=10$, symmetrical with reference to the interhemispheric fissure. The mean relative vascular volume is given in Supporting Information, SM3 for all voxel sizes and all samples. Figure 8 displays the corresponding boxplots for three sizes of isotropic imaging-voxel (150, 300, and 500 μm) and for four samples, #4 and #5 and their homologues in the contralateral hemisphere, #14 and #15. These samples are particularly interesting as they all comprise two grey-matter regions and one white-matter region in between. An exhaustive view of the boxplots for all samples is provided in Supporting Information, SM4.

Thickness and volume of the samples

One interesting parameter used in many studies in relation with brain development, plasticity and aging is the local grey-matter thickness [Kim et al., 2015]. Table II presents thickness measurements (see the section "Measurement of regional thickness" and Fig. 5b for more explanations) and volumes for sample regions where a clear orientation was identified for penetrating vessels. Only the top grey-matter regions have been kept as the bottom regions were generally incomplete. The high standard deviation around the mean vascular volume and the small number of samples made caution necessary when interpretating the comparisons. Nevertheless, no link could be established between cortical thickness and relative vascular volume ($P=0.12$). No difference was found in the mean cortical grey matter thickness between the two hemispheres. Considering both hemispheres, thickness varied from 0.958 to 2.294 mm ($n=14$, mean thickness $=1.50\pm0.34$ mm) which is in agreement with literature data for the marmoset cortex (calcarine area 17) (Fritschy and Garey, 1986; Missler et al., 1993; Pomeroy et al., 2008). This result strengthens our confidence in the methodology currently used for the measurement of cortical thickness. White-matter regions were smaller than grey-matter ones (Table II) and had a mean thickness of 0.70 ± 0.30 mm. The standard deviation observed for each of the white matter region thickness was quite large due to the definition used for the white hull (*cf*. Supporting Information, SM2.2). As the volumes extracted were strongly related to the thickness, they show the same trend. The ratio $\text{thickness}_{\text{grey}}/\text{thickness}_{\text{white}}$ for pairs of regions from each sample varied from 1.3 to 3.4 with a mean value of 2.3. No relation was found between white-matter thickness and relative blood vessel volume ($P=0.6$).

Relative vascular volume in the cerebral lobes

Laminar and areal vascularization may show different densities and patterns in monkeys (Fonta and Imbert, 2002; Keller et al., 2011; Weber et al., 2008; Zheng et al., 1991). As it does not seem sensible to analyses vascular volumes at the areal level (cf. limits in Fig. 1), we compared relative vascular volume distributions among the frontal, occipital, temporal, and parietal zones, each possibly grouping several cortical areas, with a high similarity between the two cerebral hemispheres (Table I). Samples from homologous zones of both hemispheres were pooled and the compositions of the lobes were the following:

- Frontal: grey matter 1 for samples #8, #9, #18, and #19.
- Occipital: grey matter 1 and 2 for samples #2, #12, #5, and #15, and grey matter 1 for samples #6, #16, #7, and #17.
- Temporal: grey matter 1 for samples #10 and #20.
- Parietal: grey matter 1 for samples #3 and #13.

A maximum difference of 30% can be seen among the mean relative vascular volumes in the zones, the highest values being found for the temporal zone and the lowest for the frontal zones (Table III). We found no significant difference between any of the zones for imaging-voxel sizes larger than 400 μm (not shown). On the contrary, for smaller sampling size, significant differences were found among almost all zones, except for temporal/parietal ones.

We also compared the two anatomofunctional parts of the primary visual cortex and found that the mean relative vascular volume was higher in the operculum ($2.12\%\pm0.54$, $n=6$) than in the calcarine cortex ($1.88\%\pm0.58$, $n=7$). As in the comparisons between cortical zones, vascular volumes appeared significantly different for voxel sizes below 400 μm (data not shown). Unfortunately, such comparisons are not documented for adult monkeys in either the marmoset [Fonta and Imbert, 2002] or the macaque [Weber et al., 2008].

Relative vascular volume in grey matter

The mean relative vascular volume in the grey matter calculated in the whole regional volume (i.e., without imaging-voxel sampling) varies from 1.1% to 2.6% with a mean of $1.9\pm0.5\%$ (cf Supporting Information, SM3, Global density column). When using imaging-voxels, the mean relative vascular volume is not affected by imaging-voxel size, which is to be expected, but reflects the

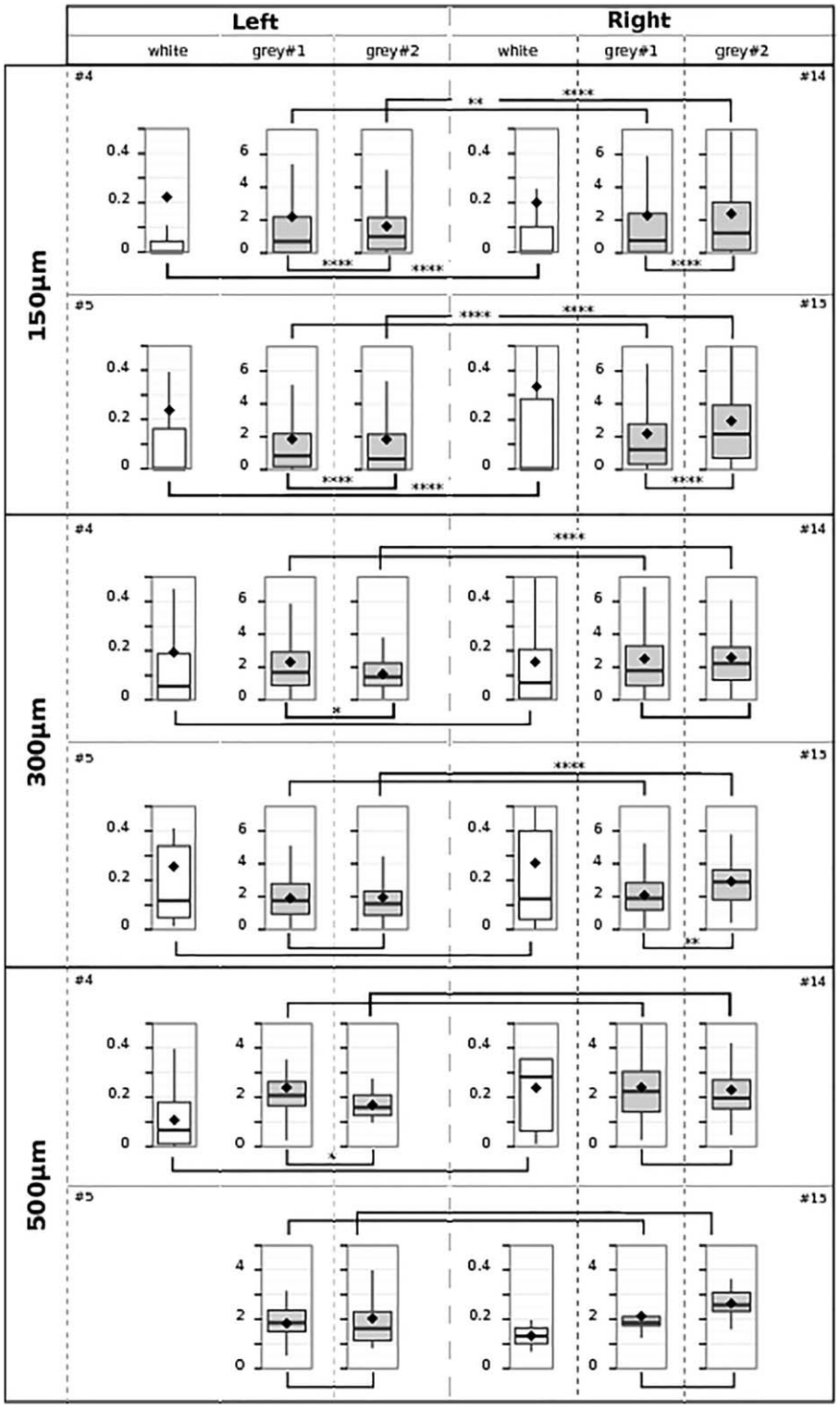

Figure 8.

Relative vascular volume (expressed in percentage of the tissue volume) distribution for various voxel sizes (150, 300, and 500 µm) in 4 samples (homolog samples in the left (4, 5) and in the right (14, 15) hemispheres). Kruskall Wallis nonparametric test is materialized by straight links between boxplots. Legend for links: *$P < 0.05$; **$P < 0.005$; ***$P < 0.001$; ****$P < 0.0001$; no asterisk, $P > 0.05$. Boxplot components: lower hinge represents 25th percentile, median represents 50th percentile, upper hinge represents 75th percentile, lower (or upper) whisker represents smallest (or largest) observation greater (or lower) than or equal to lower hinge $-$ 1.5 $\times$ IQR (or upper hinge + 1.5 $\times$ IQR), where IQR is the distance between the first and third quartiles; mean value is indicated by a diamond shape.

TABLE II. Thickness and volume of different grey-matter and white-matter regions

Sample #	Region	Thickness (mm)	Volume (mm^3)
01	Grey#1	1.519 ± 0.950	0.952
02	Grey#1	1.130 ± 0.834	1.192
-	White	0.329 ± 0.396	0.306
03	Grey#1	1.600 ± 0.991	1.180
-	White	0.629 ±0.521	0.388
04	Grey#1	1.623 ± 0.878	1.242
-	White	1.273 ± 0.834	0.915
05	Grey#1	0.958 ± 0.663	0.763
-	White	0.413 ± 0.362	0.302
08	Grey#1	1.588 ± 1.274	1.574
-	White	0.821 ± 0.683	0.790
09	Grey#1	2.294 ± 1.390	1.645
-	White	0.692 ± 0.529	0.395
10	Grey#1	1.896 ± 1.251	1.433
11	Grey#1	1.640 ± 1.320	1.764
-	White	0.727 ± 0.655	0.613
12	Grey#1	1.086 ± 0.767	1.032
-	White	0.441 ± 0.335	0.404
13	Grey#1	1.535 ± 0.922	1.296
14	Grey#1	1.395 ± 0.965	1.257
-	White	0.950 ± 0.720	0.903
18	Grey#1	1.399 ± 1.248	1.435
20	Grey#1	1.334 ± 1.101	1.409

influence of sampling edge effects when imaging-voxels are close to the borders of regions (cf. "Image Acquisition and Preprocessing"). However, when imaging-voxel size decreases, even if the mean volume is very slightly affected, the volume distribution is strongly influenced by the imaging-voxel size, as shown by the increase of the variance in Figure 8. This change in relative vascular volume distribution is more impressively depicted in Figure 9 (left column), where the contributions of all same-sized voxels from grey-matter regions found in the whole collection of 20 samples are pooled. It can be clearly observed on these histograms that the relative vascular volume is broadly distributed, with a stretched tail when sampled with 150 μm imaging-voxels. Nevertheless, as the size of the imaging-voxel becomes larger, the distribution progressively peaks generating a bell-shape-like distribution. This is nothing more than a practical illustration of a known effect, the so-called central limit theorem, which asserts that the sum of a large number of relative vascular volumes should follow a Gaussian distribution. The larger the sample inside each imaging-voxel (i.e., the larger the number of independent contributions to vascular volume), the better the Gaussian curve. It is interesting to foresee the immediate practical consequences of this effect: as relative vascular volume becomes more variable as the imaging-voxel size decreases, it becomes difficult to compare relative vascular volume from one place to another in the cortical tissue. Also, the smaller the imaging-voxel size, the larger the gap between median and mean value, and the larger the statistical difference. To calibrate the influence of sampling size on vascular volume comparisons, we compared the distributions obtained from various sampling sizes when all the left and right hemisphere samples were pooled. We found that relative vascular volume could be considered homogeneous from 500 μm voxels (Table IV).

We now proceed with the comparison between samples of the left and right hemispheres for the different imaging-voxel sizes (see Supporting Information, SM4 for a complete set of results). The global density indicates a higher CBV in the right hemisphere than in the left one (SM3). However, considering individual pairs of samples, we found that, in six pairs of samples (mainly extracted from frontal or temporal cortex), the left hemisphere showed a higher vessel density for voxel size ranging from 150 × 150 × 150 μm^3 to 1 mm^3. In the four other cases, two close samples in the occipital cortex (mainly area 17, samples 2/12 and 5/15) and 2 close samples in the parietal cortex (samples 4/14 and 10/20), vessel density was higher in the right hemisphere, whichever the voxel size in general. Figure 8 illustrates the results of the statistical comparisons between left/right distributions, for upper and lower grey regions for two pairs of these four samples. Whichever side effect, for all samples, a clear trend appears for a majority of pairs: the higher the image-voxel-size, the more similar the volume distributions. For a 150 μm imaging-voxel size, the distributions are very significantly different for each pair tested. For a 300 μm imaging-voxel size, the distributions are comparable for the vast majority of pairs (Supporting Information, SM4). We also performed a systematic bilateral comparison between left and right hemispheres by pooling all the samples from each hemisphere. Figure 10 provides the results of such bilateral comparisons for isotropic imaging-voxel sizes ranging from 150 to 1000 μm. It appears that relative vascular volume distributions in the grey matter become comparable

TABLE III. Statistical comparisons of relative vascular volumes between different cortical zones for both hemispheres, for small imaging-voxel sizes

150 μm	Frontal	Occipital	Temporal	Parietal
Frontal	$\bar{d} = 0.020$	***	***	***
Occipital		$\bar{d} = 0.022$	***	***
Temporal			$\bar{d} = 0.025$	NS
Parietal				$\bar{d} = 0.022$
250 μm	Frontal	Occipital	Temporal	Parietal
Frontal	$\bar{d} = 0.020$	***	NS	NS
Occipital		$\bar{d} = 0.022$	***	*
Temporal			$\bar{d} = 0.025$	NS
Parietal				$\bar{d} = 0.024$
400 μm	Frontal	Occipital	Temporal	Parietal
Frontal	$\bar{d} = 0.020$	NS	NS	NS
Occipital		$\bar{d} = 0.022$	NS	NS
Temporal			$\bar{d} = 0.026$	NS
Parietal				$\bar{d} = 0.023$

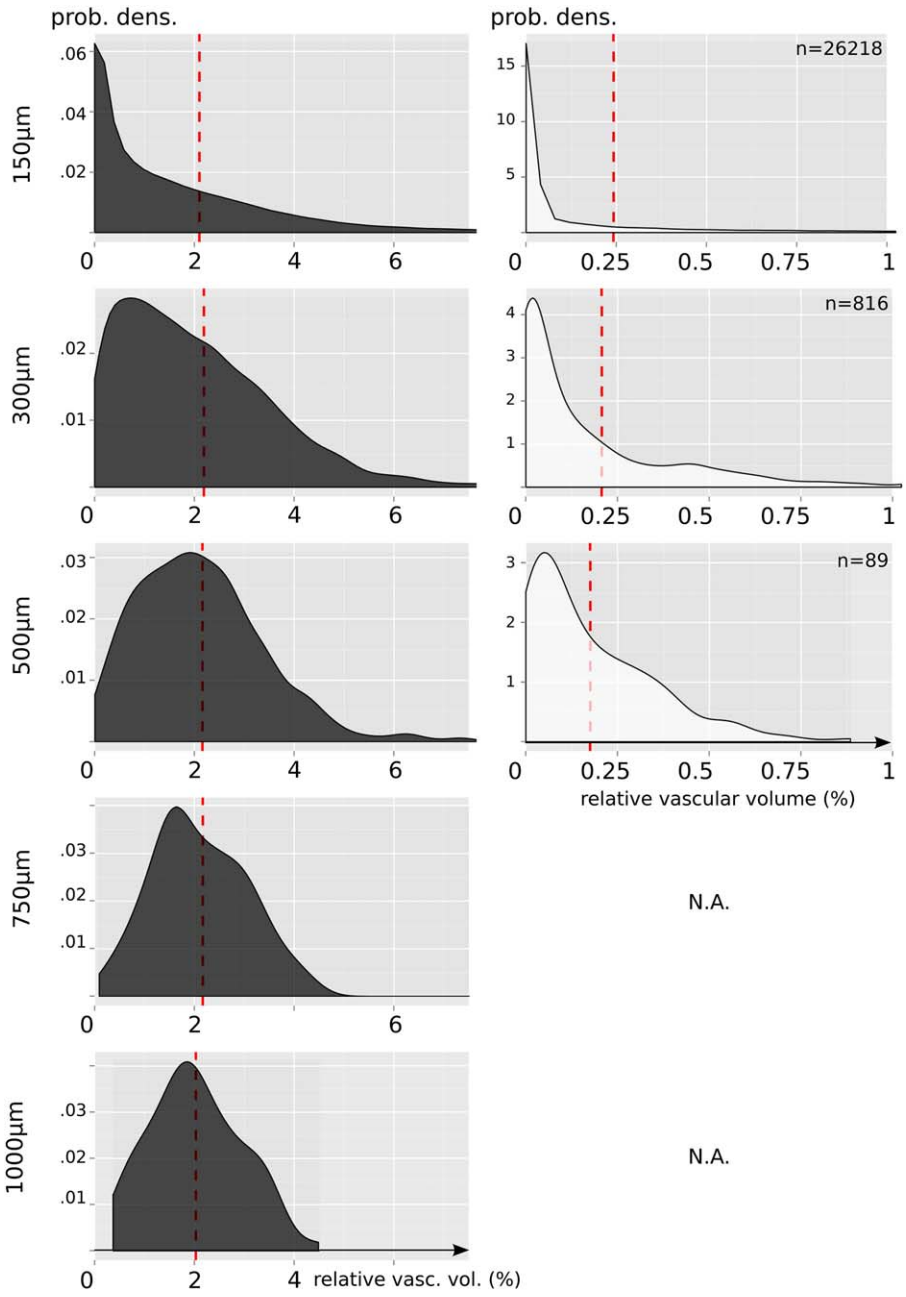

Figure 9.

Probability density functions (pdf) corresponding to relative vascular volume (abscissa, expressed in percentage) extracted from grey- (left column) and white (right column)-matter regions, according to imaging-voxel sizes (by row, 150, 300, 500, 750, and 1000 µm). The vertical dashed lines indicate mean values of relative vascular volumes for each imaging-voxel size, which do not change with imaging-voxel size, consistently with the values reported in Supporting Information, SM3. The data have been pooled for all cortical zones and both hemispheres. [Color figure can be viewed at wileyonlinelibrary.com]

between the two hemispheres for imaging-voxel sizes as large as 1000 µm. This conclusion does not arise from lack of statistics since, as given in Figure 10, for 1000 µm, n is larger than 30, and furthermore, various robust tests have been used.

Relative vascular volume in white matter

Eleven white-matter regions were segmented and used for small-size imaging-voxels (150–500 µm). For sizes

TABLE IV. Comparison of relative vascular volume between imaging-voxel sizes (all measurements pooled)

Size (μm)	150	300	500	750	1000
150	x	***	***	***	***
300		x	***	*	NS
500			x	NS	NS
750				x	NS

larger than 500 μm, only a few regions provided data for the analysis of voxel size effect. The region segmentation method used for the white matter was affected by some edge effects, the segmented regions being smaller in the middle and larger near the boundary, as can be observed in Supporting Information (SM2.2 and SM2.3). This region segmentation could affect the vascular volume estimate, especially for the smallest imaging-voxels. It seems more reliable for larger imaging-voxels.

The global relative vascular volume (without imaging-voxel sampling) in white matter regions was $0.35 \pm 0.1\%$ with slight variations depending on the sample (minimum was 0.2% and maximum was 0.6%, $n = 11$). It was ~5 times (between 1.5 and 7.5 times) smaller than that in grey-matter regions (see Supporting Information, SM3, Global density column). It appeared higher in the right hemisphere ($0.401\% \pm 0.129$) than in the left one ($0.322\% \pm 0.105$). It is worth mentioning that the average relative vascular volume obtained for white matter regions (by averaging together the mean values obtained in each region) differed from the average relative vascular volume given by the mean obtained by pooling data from all regions (the mean associated with the histograms of the right column of Fig. 9).

Considering all the samples, the mean global relative vascular volume (0.35%) was higher than the mean of mean volumes per imaging-voxel size (0.28, 0.24, and 0.18% for 150, 300, and 500 μm, respectively): the global density overevaluated the vascular volume because the

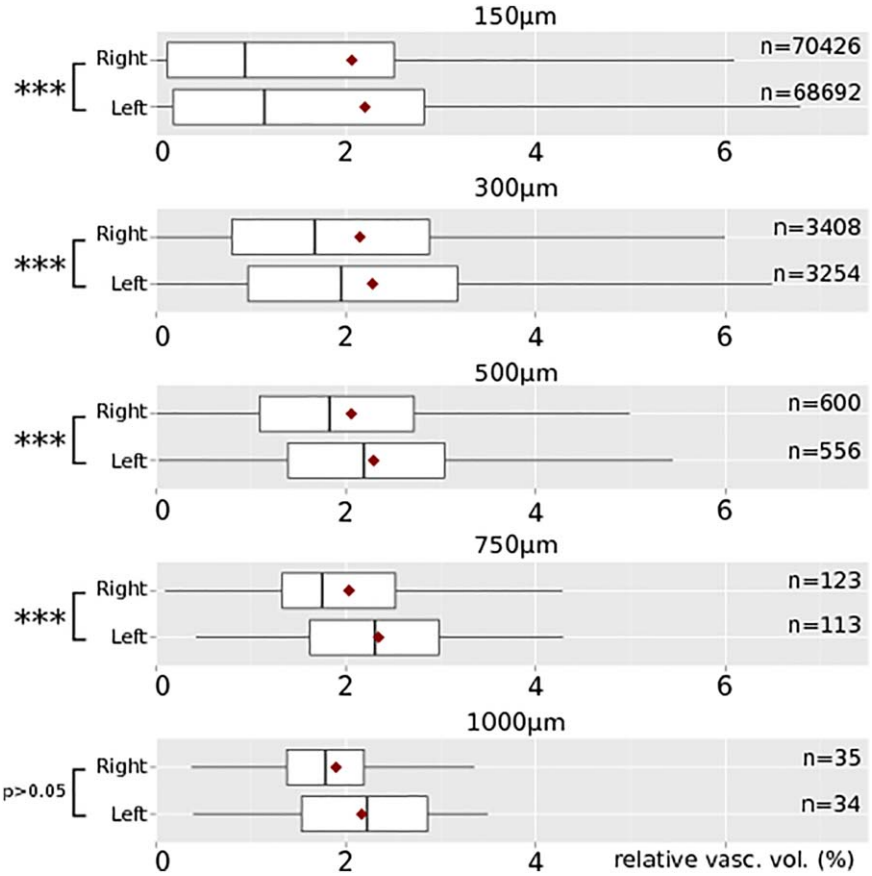

Figure 10.

Left and right hemisphere relative vascular volume boxplot according to imaging-voxel size (150, 300, 500, 750, and 1000 μm). *n* is the number of imaging voxels used for the test. Statistical comparisons between hemispheres are shown on the left. Boxplot components: same legends as Fig. 8. [Color figure can be viewed at wileyonlinelibrary.com]

shapes of white-matter region hulls comprised "high" values on the frontiers with grey-matter regions. The two hemispheres were similar for imaging-voxel sizes below or equal to 250 μm and different for 300 μm imaging-voxels. Comparisons could not be performed for larger voxels (too few samples).

Because volumes and thicknesses of white-matter regions were smaller than those of grey-matter regions (Table II), the aliasing effect occurring on measurement was slightly perceptible with respect to the mean variation observed with the voxel-size change. Regarding the variation of the density distribution calculated on the whole set of white-matter regions, the same trend was observed as in grey-matter regions: the relative vascular volume was broadly distributed, with a peak shifting toward the mean value as the size of the imaging-voxel increased. However, while this peak matched the mean and the probability density function (pdf) with a symmetric-like distribution for a 500 μm imaging-voxel in grey-matter regions, the pdf remained largely asymmetric and the maximum distant from the mean value for white-matter regions (Fig. 9).

A significant positive correlation ($P = 0.02$) was found between global relative vascular volumes in grey and white matter. This correlation decreased as the size of the imaging-voxel increases.

Influence of Voxel Orientation

Influence of voxel orientation on relative vascular volume

This section concentrates on the grey-matter regions. Only samples for which a clear perforating vessel orientation was observed were considered (cf. the section "Evaluation of sample orientation" for details). Hence, we kept 11 from left and right hemispheres to investigate the possible effect of anisotropic imaging-voxel orientation on relative vascular volume sampling. Figures 11 and 12 both show the influence of the relative imaging-voxel orientation with respect to the orientation θ of the penetrating vessels for different imaging-voxel sizes and ratios, but Figure 11 displays the results for all samples pooled together (average and variance), whereas Figure 12 illustrates the behavior of one single Sample #18.

The missing plots in Figure 11 associated with imaging-voxel size 1000 μm and aspect ratio 2.5 and 3 are not provided because the number of measurements was not sufficient to provide a relevant trend over the entire range of θ values. Also, for the sake of brevity and relevance, we only showcase certain imaging-voxel sizes, although we explored an entire set of sizes given in Supporting Information, SM5.

As shown in Figure 11, when considering all samples together, the total variation (difference between maximum and minimum value of $A_d(\theta)$) reaches 20% above the orientation-averaged value when there is alignment between imaging-voxels and the penetrating vessels (i.e., $\theta \simeq 0°$) for all the imaging-voxel sizes. This mean increase can reach 35% for the largest imaging-voxel aspect ratios. Unexpectedly at first sight, the largest anisotropy is not found between orientation $\theta = 0$ and $\theta = 90°$ but rather between $\theta = 0$ and $\theta \simeq 55°$. We believe this is associated with the contribution of pial matter, which provides supplementary blood vessel sampling when voxels are parallel to the pial surface, as further discussed below. This over-average density value progressively reaches the normal value as θ increases to 40°. Our measurements show that the larger the imaging-voxel size, the larger the orientation effect for a given aspect ratio. Furthermore, the more elongated the imaging-voxels are (i.e., the larger the aspect ratio), the more pronounced is the orientation effect for a given imaging-voxel size. By closely analyzing the behavior of each individual sample with respect to this orientation effect, we found that some of them could exhibit higher differences, up to 50%, while others might not present such an alignment effect at all. The influence of orientation is illustrated for Sample #18 in Figure 12.

Finally, it is interesting to note that the orientation effect is also observed for isotropic imaging-voxels (for which the aspect ratio equals one), which might not be particularly surprising, considering the fact that cubic voxels also present an orientation. If their size is larger than the typical distance between penetrating vessels, some orientation influence could be expected. This comment is consistent with the lack of orientation effect for the smallest imaging-voxel size, equal to 250 μm, this size being smaller than the typical distance between penetrating vessels (≃300–400 μm in the marmoset cortex [Risser et al., 2009]).

A secondary and more moderate effect is also observed when imaging-voxel orientation is parallel to the pial surface, that is, $\theta \simeq 90°$ (for samples where pial matter vessels are present). The observation that the influence of penetrating vessels is more pronounced than that of pial vessels could be explained by the fact that, although their volumes are larger, pial vessels are reticulated, with all possible orientations over the entire pial surface. In this case, sampling their influence in one given direction implies taking various pial vessel contributions with no specific synergic contribution to the overall vascular volume.

Influence of voxel orientation on magnetic perturbations

To better infer the consequences of this anisotropic sampling of the CBV for the fMRI signal, we also evaluated the magnetic perturbation associated with susceptibility contrast between vessels and tissues, in a first simplified approach. Penetrating vessels are locally approximated by infinite straight tubes having homogeneous susceptibility, as described in the section "**Estimation of Magnetic Field Inhomogeneity From the Presence of Penetrating Vessels**". Figure 13 provides an estimate of the angular anisotropy $A_B(\theta)$ of the dimensionless magnetic

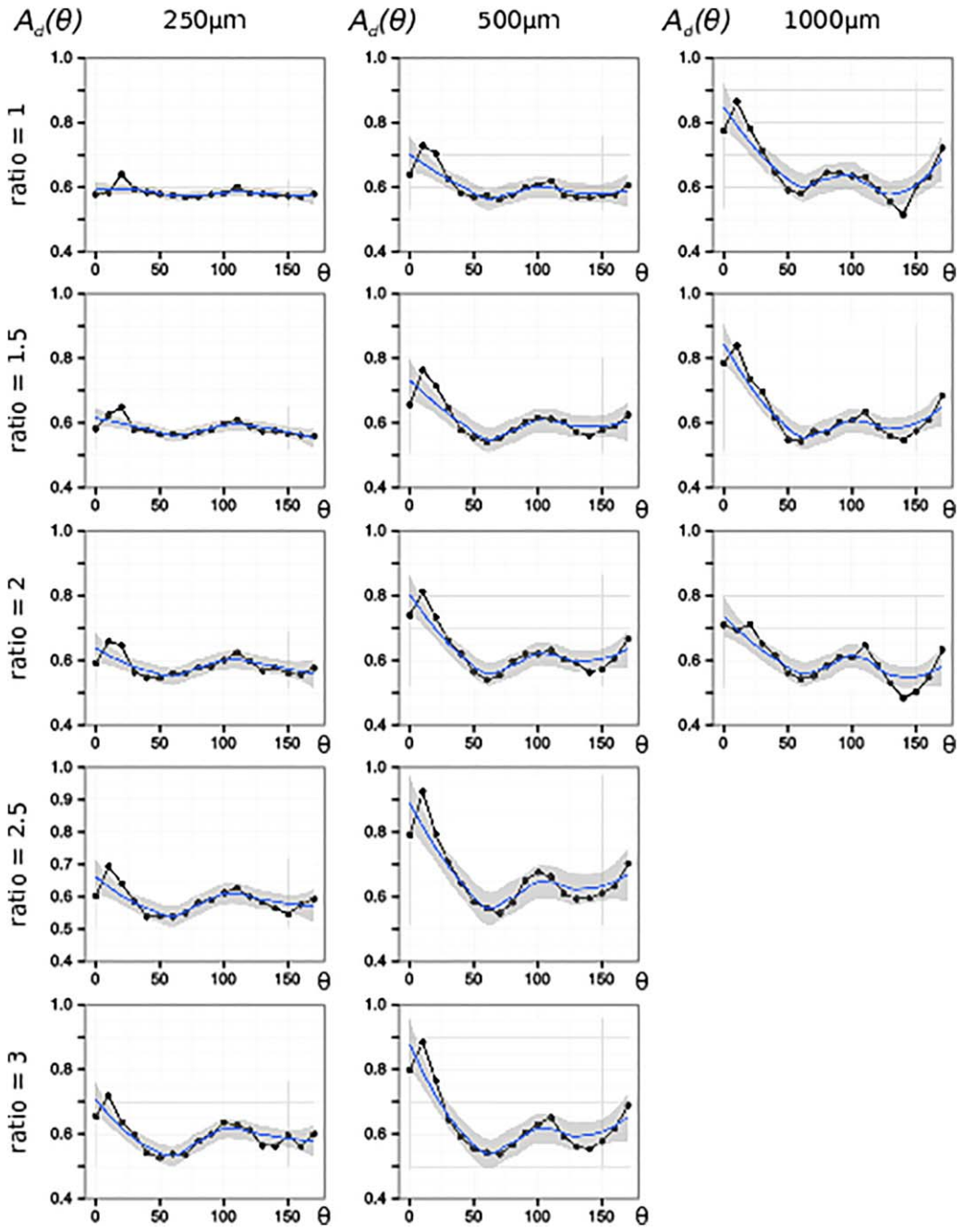

Figure 11.

Orientation anisotropy of relative vascular volume evaluated from the normalized relative quantity $A_d(\theta)$ when varying the voxel aspect ratio (vertically) and the voxel size (horizontally), where θ was the angle between the voxel- and the penetrating vessel orientation. $A_d(\theta) = (\langle d(\theta)\rangle_\varphi - \langle d\rangle_{\theta,\varphi})/\langle d\rangle_{\theta,\varphi}$ where the average relative vascular volume $\langle d(\theta)\rangle_\varphi = \int_0^{2\pi} d(\theta,\varphi)d\varphi$ and the average relative vascular volume $\langle d\rangle_{\theta,\varphi} = \int_0^{\pi} \sin\theta \langle d(\theta)\rangle_\varphi d\theta$. Analysis was performed with 11 grey-matter samples. Smooth blue lines represent polynomial regressions of $A_d(\theta)$ (black lines) and θ variation with the associated standard error as a grey wrapper. [Color figure can be viewed at wileyonlinelibrary.com]

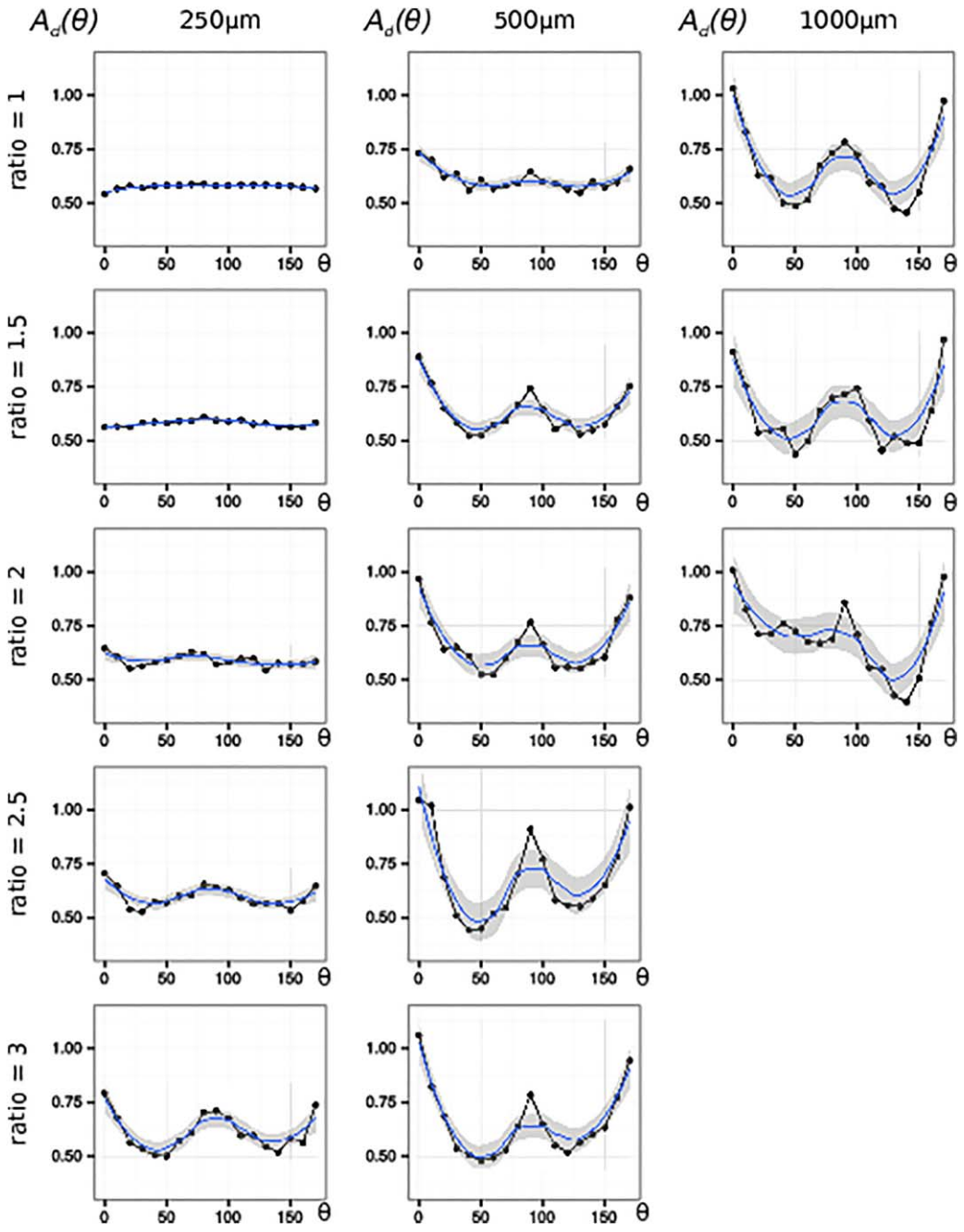

Figure 12.

Orientation anisotropy of relative vascular volume evaluated from the normalized relative quantity $A_d(\theta)$ when varying the voxel aspect ratio (vertically) and the voxel size (horizontally), where θ was the angle between the voxel- and the penetrating vessel orientation. Same convention as Figure 11 considering the grey-matter region found in Sample # 18. [Color figure can be viewed at wileyonlinelibrary.com]

perturbations, to quantify the dependence of the magnetic tissue response on the orientation angle θ between the penetrating vessel preferential direction and the imposed static magnetic field $\mathbf{B}_0$. If the magnetic perturbations were isotropic, that is, if the presence of vessel locally deform the imposed static field in every direction in space, $A_B(\theta)$

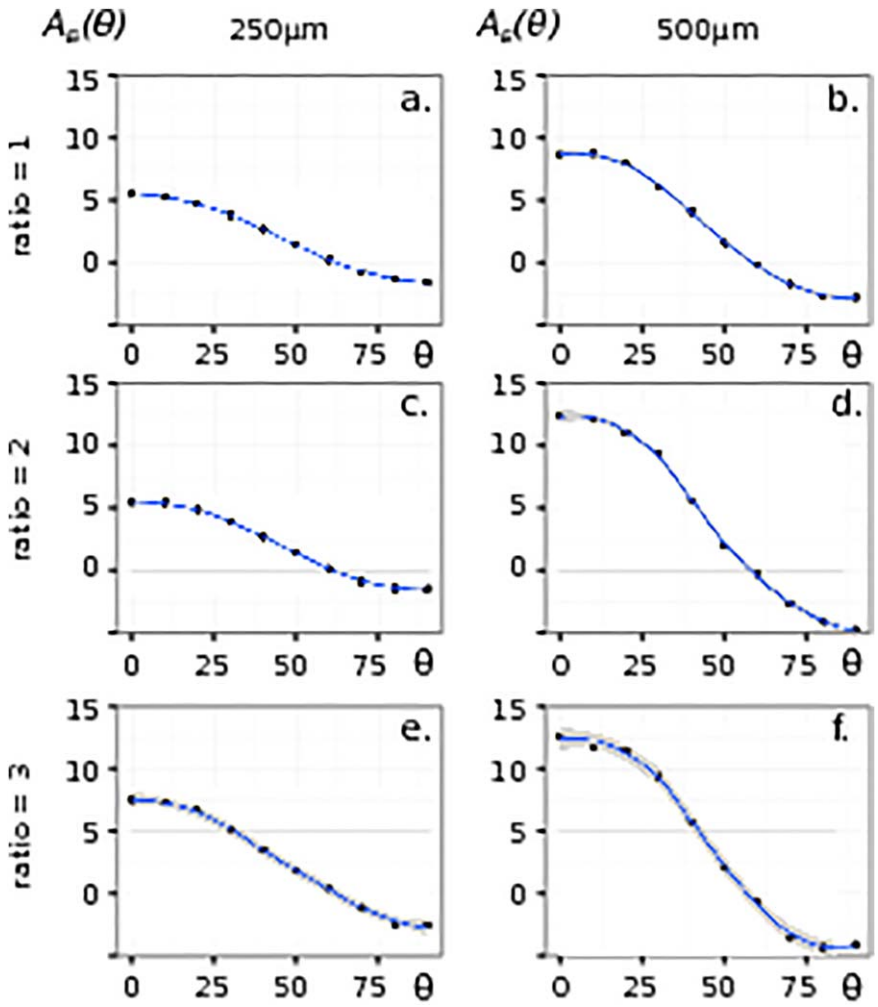

Figure 13.

Orientation-linked anisotropy of magnetic perturbation, averaged within each imaging-voxel, evaluated from quantity $A_B(\theta)=(\langle\frac{\delta B}{B_0}(\theta)\rangle_\varphi-\langle\frac{\delta B}{B_0}\rangle_{\theta,\varphi})/\langle\frac{\delta B}{B_0}\rangle_{\theta,\varphi}$ where the average magnetic perturbation is $\langle\frac{\delta B}{B_0}\rangle_{\theta,\varphi}=\int_0^\pi \sin\theta\langle\frac{\delta B}{B_0}(\theta)\rangle_\varphi d\theta$ and where θ is the angle between the penetrating vessel orientation and the magnetic field $\mathbf{B}_0$ direction (or the imaging-voxel orientation). The relative angular variation of the magnetic signal indicates the strength of the expected anisotropy. A susceptibility contrast of $\Delta\chi = 10^{-7}$ IU has been chosen. (**a**) $\langle\frac{\delta B}{B_0}\rangle_{\theta,\varphi} = 1.3e^{-10}$, (**b**) $\langle\frac{\delta B}{B_0}\rangle_{\theta,\varphi} = 7.9e^{-11}$, (**c**) $\langle\frac{\delta B}{B_0}\rangle_{\theta,\varphi} = 1.3e^{-10}$, (**d**) $\langle\frac{\delta B}{B_0}\rangle_{\theta,\varphi} = 5.8e^{-11}$, (**e**) $\langle\frac{\delta B}{B_0}\rangle_{\theta,\varphi} = 1.0e^{-10}$, (**f**) $\langle\frac{\delta B}{B_0}\rangle_{\theta,\varphi} = 5.2e^{-11}$. [Color figure can be viewed at wileyonlinelibrary.com]

would be almost constant, within some statistical fluctuations. The observed variation of $A_B(\theta)$ shows the marked angular anisotropy between the aligned case $\theta = 0$ and the case of $\theta = \pi/2$ in Sample #18. The mean magnetic perturbation reaches 500% of the orientation-averaged value when there is alignment between the imaging-voxels (or $\mathbf{B}_0$) and the penetrating vessels for isotropic voxels. From Figure 13, one can observe that for all aspect ratios between 1 and 3, the total variation of $A_B(\theta)$ rises 650% for 250 µm imaging-voxels up to 1600% for 500 µm imaging-voxels. This trend exceeds the aforementioned CBV anisotropy (i.e., between 25% and 50%, see Fig. 12) by a factor 20, showing that the magnetic response is much more sensitive to orientation of penetrating vessels than vascular volume. Of course, the regular sinusoidal shape of Figure 13 results from the influence of quasi-parallel penetrating vessel on the local magnetic field, whilst ignoring capillary contributions. This is in opposition to the results on CBV presented in Figures 11 and 12, where all vessel contributions have been included. As capillaries represent half of the cortical microvascular volume, it can be considered that half the isotropically distributed magnetic susceptibility contrast is neglected when ignoring their contribution. Hence, for Sample #18 imaged with a 500 µm imaging-

voxel having an aspect ratio of 1:3, one should roughly expect 800% variation of the magnetic perturbation response between imaging-voxels aligned with or, on the contrary orthogonal to, penetrating vessels. Thus, our results indicate that we expect the CBV anisotropy response to be 16 times smaller than the magnetic one. Using this estimation from the perspective of the CBV anisotropy results associated with the entire set of samples analyzed in Figure 11, we can infer that, on average, for anisotropic 500 μm voxels having an aspect ratio of 1:3, as 35% anisotropy is found in CBV, we expect an average of 560% anisotropy in the magnetic response, which is a sizeable effect.

DISCUSSION

We analyzed the CBV distribution in the grey and white matter, and in various cortical areas, in both cerebral hemispheres of a marmoset monkey. The CBV verages 1.9% in the grey matter and 0.36% in the white matter, which is comparable to data in the literature (about 1–2% in rodents and in monkeys [Tsai et al., 2009]). A value of 2.7% has been reported for the temporal cortex from a postmortem study on humans [Lauwers et al., 2008]. Measurement after labeled xenon inhalation indicates a mean value of 3 ml/100 mg brain/min [Meyer et al., 1978]. PET and MRI measurements provide higher values (4.7–5%) in human cortical gray matter when CBV is around 2–2.7% in the white matter [Hatazawa et al., 1995; Jensen et al., 2006; Leenders et al., 1990). Therefore, in vivo brain imaging may give (i) higher values than high resolution methodologies applied to larger voxel sizes (e.g., CT microtomography, confocal microscopy) and (ii) high vascular volume values for the white matter. This could be explained by differences in the image characteristics, especially the contribution of macrovessels which are ignored when considering small voxels inside grey matter. Furthermore, a better contrast between tissue and vascular compartment provides more reliable segmentation when using high-resolution methods. Similarly, differentiation between grey and white matter is particularly delicate at the white-grey matter junction, which may lead to misregistration of the white and grey matter regions for in vivo brain imaging. Histological approaches, which generally report CBV ratio from 2 to 3 between grey and white matter in humans [Ballabh et al., 2004; Brown et al., 2007; Lierse and Horstmann, 1965), use small sized samples and cannot appreciate the scale-dependent organization of the vascular network [Risser et al., 2007]. Thus, difference in vessel and tissue identification, and sampling size, may explain the variance in the results between the different studies.

The global relative vascular volume (without sampling) was comparable in the right and left hemispheres, for both grey (1.98% vs 1.88%) and white matter (0.40% vs 0.32%). We did not find any significant difference in the global relative vascular volumes between cortical zones corresponding to the cerebral lobes.

However, these results, corresponding to low-resolution imaging, could hide some disparities that would be revealed by high-resolution imaging. Thus, comparative analyses for grey matter with imaging-voxels smaller than 1 mm^3 showed that relative vascular volume was significantly higher in the left hemisphere. Interestingly, an anatomical temporal lobe asymmetry has been reported in the marmoset [Heilbroner and Holloway, 1988]. However, it is important to stress that bilateral comparisons are usually dedicated to symmetrical areas or regions. CBF measured in normal resting subjects was found to be significantly higher in the left hemisphere, when comparing symmetrical regions in both hemispheres [Meyer et al., 1978]. Human brain structural lateralization has been described in terms of gray matter volume, cortical thickness, cortical surface area, and network topology in the white matter [Hervé et al., 2013; Maingault et al., 2016; Takao et al., 2011; Zhong et al., 2017]. Such lateralization could be due to asymmetries at the microstructural level, such as cell size, minicolumn spacing, width, and number [Chance, 2014; Hutsler and Galuske, 2003). Independently or in close association with the neuronal organization, vessel density could also contribute to the structural and the functional asymmetry of the cortex.

Furthermore, CBV differences between the frontal, occipital, temporal, and frontal cortical areas rise if imaging-voxel sizes are smaller than 400 μm. More generally, our study points out that CBV cannot be considered homogeneous among voxels in a whole-brain image, if these voxels are smaller than 300 μm. This is consistent with previous findings associated with blood flow modeling in grey matter. By analyzing the underlying vascular hemodynamic couplings of penetrating vessels through their vascular perfusion territories, connecting with one another over large distances, Guibert et al. [2012] have shown that their functional influence can spread over large distances. A typical radius of 380 μm of vascular perfusion territory around each penetrating arteriole was found [Guibert et al., 2012], and it is consistent with the imaging-voxel size of 400 μm for which homogeneity between areas has been found. This effect is obviously statistically expected, as already mentioned in the Results section. Consequently, median and standard deviation of CBV absolute values differ according to imaging-voxel size. For example, from 150 μm to 1 mm, pooling all measurements, the median changed from 1% to 2% and the standard deviation from 4% to 0.9%. As comparative functional analyses are highly dependent upon the resolution of the image acquisition and/or analysis, we now discuss the possible practical consequences of these findings.

These results challenge several functional imaging modalities as they pursue an increase in their spatial resolution. This is especially true when we consider the need to evaluate intrinsic functional local properties rather than

relative ones, by subtracting the local baseline. Bilateral comparisons are routinely used for brain cancer detection, particularly by using a PET scan (e.g., Jain [2011]). We expect such comparison to become noisier because of CBV heterogeneity, when voxel sizes are downscaled. This consideration can affect the interest of high resolution for early detection of brain cancer, since false positives or, on the contrary, false negatives could result from CBV variations. Static CBV heterogeneity will also footprint the entire spatiotemporal correlation patterns found between different imaging-voxels: high CBV in two distinct imaging-voxels will produce structural (and not necessarily functional) correlation, while, on the contrary, distinct (high and low) CBV in two different imaging-voxels might produce (again, not necessarily functional) anticorrelation. Hence, CBV heterogeneity might produce possibly inexistent neurofunctional links, not necessarily ruled out from substracting the baseline, as described and observed in gradient-echo fMRI [Ogawa et al., 1990]. It has been acknowledged in the literature that vascular response to neuronal activity should probably vary between cortical areas [Logothetis and Wandell, 2004].

By confronting BOLD-fMRI with electrophysiological measurements, Devonshire et al. [2012] found direct experimental evidence to question the homogeneity of the functional response in the subcortical structure of rat brain. Furthermore, using direct optical imaging of thinned-skull windows in mouse brains, with simultaneous electrophysiological recordings, Huo et al. [2014] found that CBV could either increase with neuronal activity or, in contrast, remain stationary, depending on the cortex area, especially in the frontal lobes. This observation reveals a supplementary functional heterogeneity in neurovascular response (mainly associated with diameter change of penetrating vessels). Huo et al. [2014] also found heterogeneous CBV in different cortex areas, but most of their results were discussed after subtracting baseline CBV. Our results suggest that, at high resolution, the differences observed in CBV will generalize to most cortical areas, as suggested by Table III. Nevertheless, a detailed quantitative interpretation of the reported findings to fMRI imaging is far beyond the scope of this study. Indeed, the contribution of physiological parameters, especially cerebral flow, into the baseline magnetic resonance imaging is a delicate and complex issue [Kim and Ogawa, 2012]. The various levels of the vascular tree organization distinctly affect the MR signals, depending on the chosen sequence. For BOLD-FMRI, it is known that veins predominantly affect the relaxation frequencies R1* and R2*, so that veinous contribution of CBV has to be considered [Kim and Ogawa, 2012]. As one-third of penetrating vessels are veins (Guibert et al. [2012] and reference therein), and penetrating vessels represent half of the CBV [Risser et al., 2009], we expect 1/6 of CBV to be associated with veins. Furthermore, as capillary contribution to CBV anisotropy is negligible, we expect 1/3 of the reported CBV anisotropy to be associated with veins. From Figure 11, we infer that for in-plane imaging-voxels size $500 \times 500\ \mu m^2$, having aspect ratio 2, or 2.5, an average 8%, respectively 11.5% variation of venous baseline CBV associated with orientational effects. Referring to the linearized relation (4) of Kim and Ogawa [2012], BOLD signal changes are simply related to the venous oxygenation level change weighted by baseline venous blood volume. We then expect that the reported anisotropy affects BOLD signal by 8% and 11.5% for imaging-voxels having an aspect ratio of 2 and 2.5, respectively, as baseline venous blood volume is affected by this proportion. This estimation, however, assumes isotropic venous oxygenation level change, that is, that the oxygenation level is not influenced by the static field (or imaging-voxel) direction which is not obvious. However, these figures seem significant enough to be reported.

Furthermore, our results revealed that if the average values of relative vascular volumes (or CBV) are poorly affected by sampling voxel size, they are indeed affected by voxel orientation. Our findings show that when the imaging-voxel main axis and penetrating vessel orientation are aligned, CBV increases by an average of 20% compared to nonaligned configurations. The effect positively links to voxel size and aspect ratio, which generally corresponds to the ratio between slice thickness and pixel size in MRI acquisitions. For any voxel aspect ratio, a 30° misalignment is sufficient to suppress the observed level-off of apparent CBV. As functional imaging signals are known to increase proportionally with CBV, we expect this effect to be responsible for a significant alignment artefact, associated with the increase in the observed signal for voxels aligned with penetrating vessels. Such an effect is obviously of minor relevance when activation signals are confronted with a baseline associated with a basic state recorded at the same location with the same voxel sampling and imaging protocol. Thus, functional signals considered as relative comparisons using the same imaging modality should not be concerned by orientation effects. Nevertheless, when considering more intrinsic functional features of imaging-voxels, for example, normalized functional response computed from multimodality imaging [Friston et al., 1995], some caution is needed, especially at ultrahigh resolution, as multimodality is never provided with the same imaging-voxel size, aspect ratio, and orientation. The influence of voxel orientation could become critical for the role of vascular structure in MRI. The orientation of the static magnetic field relative to the penetrating vessels should matter, as these vessels contribute almost 50% of CBV (*cf.* Risser et al. [2009]). The results reported in the section "Influence of Voxel Orientation" indicate that (i) voxel orientation matters even for isotropic voxels, (ii) the orientation dependency is more pronounced for larger imaging-voxel sizes and aspect ratios, and (iii) the CBV exhibits a sample-average 35% angular anisotropy for 500 μm imaging-voxels with an aspect ratio of 1:3. A recent study reaches similar conclusions using CBV

measurements for 13 human subjects measuring an averaged anisotropy equal to 45% for similar aspect ratios [Hernández-Torres et al., 2016]. As all fMRI signals are proportional to the local magnetic field sampled by imaging-voxels, our results pinpoint important orientational effects that have scarcely been discussed in the literature.

Moreover, our results can be used to correct orientation bias. By estimating the angle θ between the normal direction to the cortex surface and the main axis of the imaging-voxel, it is possible to use the result of Figure 11, showing the θ-dependence of the average CBV, to systematically correct the excess from CBV sampling.

CONCLUSION

High-quality, micron-size resolved synchrotron tomography images of microvascular structures over large volumes of primate cerebral cortex have permitted a large collection of grey- and white-matter regions to be segmented by means of specific image segmentation methods. Several basic parameters (thickness, volume, and CBV) have been extracted, providing a ground-truth for their subsequent study. More specifically, we have analyzed the effect of imaging-voxel sampling for various sizes, orientations, and aspect ratios, consistently chosen from those found in the literature devoted to fMRI.

Our results indicate that, at high resolution, the homogeneity of CBV over cortical areas, lobes, or hemispheres is becoming less and less evident depending on the imaging-voxel size considered. Furthermore, our results put forward the quantitative influence of imaging-voxel anisotropy, and propose some systematic corrections for local orientation effects associated with the contributions of penetrating vessels. More generally, our results strongly suggest that the vascular anatomical substratum is becoming increasingly important as the spatial resolution of brain imaging techniques improves.

ACKNOWLEDGMENTS

The authors thank Pr. M. Rosa for providing the marmoset atlas, T. Weitkamp for his support during acquisitions at ESRF, L. Renaud for technical help in sample preparation, and R. Pellé for his valuable contribution to the histological analysis during his master internship. They also thank Florence Rémy, Jennifer Mackie, and Jean-Pierre Jaffrézou for careful reading of the manuscript.

REFERENCES

Ballabh P, Braun A, Nedergaard M (2004): Anatomic analysis of blood vessels in germinal matrix, cerebral cortex, and white matter in developing infants. Pediatr Res 56:117–124

Brown WR, Moody DM, Thore CR, Challa VR, Anstrom JA (2007): Vascular dementia in leukoaraiosis may be a consequence of capillary loss not only in the lesions, but in normal-appearing white matter and cortex as well. J Neurol Sci 257: 62–66.

Chance SA (2014): The cortical microstructural basis of lateralized cognition: A review. Front Psychol 5:820.

Devonshire IM, Papadakis NG, Port M, Berwick J, Kennerley AJ, Mayhew JE, Overton PG (2012): Neurovascular coupling is brain region-dependent. NeuroImage 59:1997–2006.

Duvernoy HM (1999): The Human Brain. Surface, Three-Dimensional Sectional Anatomy With MRI, and Blood Supply, 2nd ed. Wien, NewYork: Springer. p 491.

Fonta C, Imbert M (2002): Vascularization in the primate visual cortex during development. Cereb Cortex 12:199–211.

Fonta C, Chappert C, Imbert M (1997): N-methyl-d-aspartate subunit r1 involvement in the postnatal organization of the primary visual cortex of *Callithrix jacchus*. J Comp Neurol 386: 260–276.

Fonta C, Négyessy L, Renaud L, Barone P (2004): Areal and subcellular localization of the ubiquitous alkaline phosphatase in the primate cerebral cortex: Evidence for a role in neurotransmission. Cereb Cortex 14:595–609.

Frangi A, Niessen W, Vincken K, Viergever M (1998): Multiscale vessel enhancement filtering. In: Wells W, Colchester A, Delp S, editors. Medical Image Computing and Computer-Assisted Interventation MIC-CAI'98, Lecture Notes in Computer Science, Vol. 1496. Berlin Heidelberg: Springer. pp 130–137.

Friston K, Ashburner J, Frith C, Poline J, Heather J, Frackowiak RSJ (1995): Spatial registration and normalization of images. Hum Brain Mapp 3:165–189.

Fritschy JM, Garey LJ (1986): Quantitative changes in morphological parameters in the developing visual cortex of the marmoset monkey. Dev Brain Res 29:173–188.

Gallyas F (1978): Silver staining of myelin by means of physical development. Neurol Res 1:203–209.

Goense J, Bohraus Y, Logothetis NK (2016): fMRI mechanisms at laminar resolution: Implications for bold-models. Front Comput Neurosci 10:10.3389/fncom.2016.00,066

Guibert R, Fonta C, Risser L, Plouraboué F (2012): Coupling and robustness of vascular units in cortex. NeuroImage 62: 408–417.

Hatazawa J, Fujita H, Kanno I, et al. (1995): Regional cerebral blood flow, blood volume, oxygen extraction fraction, and oxygen utilization rate in normal volunteers measured by the autoradiographic technique and the single breath inhalation method. Ann Nucl Med 9:15–21.

Heilbroner PL, Holloway RL (1988): Anatomical brain asymmetries in New World and Old World monkeys: Stages of temporal lobe development in primate evolution. Am J Phys Anthropol 76:39–48.

Hernández-Torres E, Kassner N, Forkert ND, Wei L, Wiggermann V, Daemen M, Machan L, Traboulsee A, Li D A R (2016): Anisotropic cerebral vascular architecture causes orientation dependency in cerebral blood flow and volume measured with dynamic susceptibility contrast magnetic resonance imaging. J Cereb Blood Flow Metab DOI 10.1177/0271678X16653134

Herve PY, Zago L, Petit L, Mazoyer B, Tzourio-Mazoyer N (2013): Revisiting human hemispheric specialization with neuroimaging. Trends Cogn Sci 17:69–80.

Huo BX, Smith JB, Drew PJ (2014): Neurovascular coupling and decoupling in the cortex during voluntary locomotion. J Neurosci 34:10975–10981.

Hutsler J, Galuske RA (2003): Hemispheric asymmetries in cerebral cortical networks. Trends Neurosci 26:429–435.

Jain R (2011): Perfusion ct imaging of brain tumors: An overview. Am J Neuroradiol 32:1570–1577.

Jensen JH, Lu H, Inglese M (2006): Microvessel density estimation in the human brain by means of dynamic contrast-enhanced echo-planar imaging. Magn Reson Med 56:1145–1150.

Keller AL, Schütz A, Logothetis NK, Weber B (2011): Vascularization of cytochrome oxidase-rich blobs in the primary visual cortex of squirrel and macaque monkeys. J Neurosci 31: 1246–1253.

Kim JP, Seo SW, Shin HY, Ye BS, Yang JJ, Kim C, Kang M, Jeon S, Kim HJ, Cho H (2015): Effects of education on aging-related cortical thinning among cognitively normal individuals. Neurology 85:806–812.

Kim SG, Ogawa S (2012): Biophysical and physical origin of blood oxygenation level-dependent f-MRI signals. J Cereb Blood Flow Metab 32:1188–1206.

Lauwers F, Cassot F, Lauwers-Cances V, Puwanarajah P, Duvernoy H (2008): Morphometry of the human cerebral cortex microcirculation: General characteristics and space-related profiles. NeuroImage 39:936–948.

Leenders KL, Perani D, Lammertsma AA, et al. (1990): Cerebral blood flow, blood volume and oxygen utilization. Normal values and effect of age. Brain 113: 27–47.

Lierse W, Horstmann E (1965): Quantitative anatomy of the cerebral vascular bed with especial emphasis on homogeneity and inhomogeneity in small ports of the gray and white matter. Acta Neurol Scand Suppl 14:15–19.

Lin W, An H, Ford A, Vo K, Lee J, Zaharchuk G (2010): Imaging of Brain Oxygenation. Cambridge University Press. pp 75–88. doi: 10.1017/CBO9781139004053.007.

Logothetis N, Wandell B (2004): Interpreting the bold signal. Annu Rev Physiol 66:735–769.

Maingault S, Tzourio-Mazoyer N, Mazoyer B, Crivello F (2016): Regional correlations between cortical thickness and surface area asymmetries: A surface-based morphometry study of 250 adults. Neuropsychologia 93:350–364.

Meyer JS, Ishihara N, Deshmukh VD, Naritomi H, Sakai F, Hsu MC, Pollack P (1978): Improved method for noninvasive measurement of regional cerebral blood flow by 133Xenon inhalation. Part I: Description of method and normal values obtained in healthy volunteers. Stroke 9:195–205.

Michaloudi H, Grivas I, Batzios C, Chiotelli M, Papadopoulos GC (2005): Areal and laminar variations in the vascularity of the visual, auditory, and entorhinal cortices of the developing rat brain. Dev Brain Res 155:60–70.

Missler M, Eins S, Merker HJ, Rothe H, Wolff JR (1993): Pre-and postnatal development of the primary vi-sual cortex of the common marmoset. 1. A changing space for synaptogenesis. J Comp Neurol 333:41–52.

Negyessy L, Xiao J, Kantor O, Kovacs GG, Palkovits M, Doczi TP, Renaud L, Baksa G, Glasz T, Ashaber M, Barone P, Fonta C (2011): Layer-specific activity of tissue non-specific alkaline phosphatase in the human neocortex. Neuroscience 172: 406–418.

Ogawa S, Lee TM, Nayak AS, Glynn P (1990): Oxygenation-sensitive contrast in magnetic resonance image of rodent brain at high magnetic fields. Magn Reson Med 14:68–78.

Ogawa S, Menon RS, Tank DW, Kim SG, Merkle H, Ellermann JM, Ugurbil K (1993): Functional brain mapping by blood oxygenation level-dependent contrast magnetic resonance imaging A comparison of signal characteristics with a biophysical model. Biophys J 64:803–812.

Palazzi X, Bordier N (2008): The Marmoset Brain in Stereotaxic Coordinates. Springer.

Pannetier NA, Debacker C, Mauconduit F, Christen T, Barbier E (2013): Simulation tool for dynamic contrast enhanced MRI. PLoS One 8:499–509.

Paxinos G, Watson C, Petrides M, Rosa M, Tokuno H (2012): The Marmoset Brain in Stereotaxic Coordinates. Academic Press.

Plouraboué F, Cloetens P, Fonta C, Steyer A, Lauwers F, Marc-Vergnes JP (2004): X-ray high-resolution vascular network imaging. J Microscopy 215:139–148.

Pomeroy IM, Jordan EK, Frank JA, Matthews PM, Esiri MM (2008): Diffuse cortical atrophy in a marmoset model of multiple sclerosis. Neurosci Lett 437:121–124.

Reina-De La Torre F, Rodriguez-Baeza A, Sahuquillo-Barris J (1998): Morphological characteristics and distribution pattern of the arterial vessels in human cerebral cortex: A scanning electron microscope study. Anat Rec 251:87–96.

Risser L, Plouraboué F, Steyer A, Cloetens P, Le Duc G, Fonta C (2007): From homogeneous to fractal normal and tumorous micro-vascular networks in the brain. J Cereb Blood Flow Metab 27:293–303.

Risser L, Plouraboué F, Descombes X (2008): Gap filling of 3-D micro-vascular networks by tensor voting. IEEE Trans Med Imag 27:674–687.

Risser L, Plouraboué F, Cloetens P, Fonta C (2009): A 3d-investigation shows that angiogenesis in primate cerebral cortex mainly occurs at capillary level. Int J Dev Neurosci 27:185–196.

Shih FY (2009): Image Processing and Mathematical Morphology, Fundamentals and Applications. CRC Press.

Takao H, Abe O, Yamasue H, Aoki S, Sasaki H, Kasai K, Yoshioka N, Ohtomo K (2011): Gray and white matter asymmetries in healthy individuals aged 21–29 years: A voxel-based morphometry and diffusion tensor imaging study. Hum Brain Mapp 32:1762–1773.

Tsai PS, Kaufhold JP, Blinder P, Friedman B, Drew PJ, Karten HJ, Lyden PD, Kleinfeld D (2009): Cor-relations of neuronal and microvascular densities in murine cortex revealed by direct counting and colocalization of nuclei and vessels. J Neurosci 29:14553–14570.

Vignaud A, Rodriguez I, Ennis DB, DeSilva R, Kellman P, Taylor J, Bennett E, Wen H (2006): Detection of myocardial capillary orientation with intravascular iron-oxide nanoparticles in spin-echo MRI. Magn Reson Med 55:725–730.

Wang Y, Yu Y, Li D, Bae K, Brown J, Lin W, Haacke E (2000): Artery and vein separation using susceptibility-dependent phase in contrast-enhanced mra. J Magn Reson Imag 12:661–670.

Weber B, Keller AL, Reichold J, Logothetis NK (2008): The microvascular system of the striate and extras-triate visual cortex of the macaque. Cereb Cortex 18:2318–2330.

Zheng D, LaMantia AS, Purves D (1991): Specialized vascularization of the primate visual cortex. J Neurosci 11:2622–2629.

Zhong S, He Y, Shu H, Gong G (2017): Developmental changes in topological asymmetry between hemispheric brain white matter networks from adolescence to young adulthood. Cereb Cortex 27:2560–2570.